

# INTERNAL REPORT 263/2021

STAGE edizione 2021



*Elise Aiello*

**Istituto Nazionale di Fisica Nucleare**  
**Laboratori Nazionali di Legnaro**

*[Signature]*

*Filippo Paolone*

*Riccardo Grosso*

*Giovanni Schivo*

*Giacomo Salvadori*

*Eduardo Rada*

*Anna Rita*

*Filippo Longarelli*

*Alice Giampelli*

*Andrea Ballarín*

*Francesco Alessandrini*

*Andrea Amato*

*Gionluca Rossi*

*Matteo De Santis*

*Ilma Lacerda*

*Lorenzo Carletti*

*Alessandro Gionterio*

*Elena Caporaso*

*Fiamma Del Rio*

*Vendrame Massimo*

*Desiderio*

*Sofia Busatti*

*Giovanni Zatti*

*Helena Boffo*

*Alexander Zanussi*

*Norma Ferraresi*

*Elisa Barberi*

*Andrea Zanussi*

*Flavia Segala*

*Lise Colaneri*

*Francesca Martini*

*Ena Gatti*

*Corinne Contardo*

*Barretto Davide*

INTERNAL REPORT 263/2021

STAGE edizione 2021



**Istituto Nazionale di Fisica Nucleare**  
**Laboratori Nazionali di Legnaro**



# Rutherford Experiment: Physics, Electronics, and Informatics

L. Carletti<sup>1</sup>, R. Grasso<sup>2</sup>, C. Lanzarolo<sup>3</sup>, G. Salvadeo<sup>4</sup>, G. Schiavo<sup>5</sup>, F. Tanganelli Mateos<sup>6</sup>, G. Zatti<sup>7</sup>

<sup>1</sup>IIS Bassi-Burgatti di Cento, (Ferrara), Italy

<sup>2</sup>ITIS C. Zuccante di Mestre, (Venezia), Italy

<sup>3</sup>LS G.Cotta di Legnago, (Verona), Italy

<sup>4</sup>IIS Newton-Pertini di Camposampiero, (Padova), Italy

<sup>5</sup>LS G. Galilei di Selvazzano, (Padova), Italy

<sup>6</sup>LC L. Ariosto di Ferrara, (Ferrara), Italy

<sup>7</sup>LS A.Einstein di Piove di Sacco, (Padova), Italy

## INTRODUCTION

We performed the Rutherford experiment [1] at INFN LNL by using an alpha beam accelerated with the AN2000 accelerator. We studied the behaviour of scattered alpha particles on different targets. The goal of the experiment was to check the Rutherford scattering formula. We also used the Rutherford backscattering (RBS) technique to study thick film of deposited material.

## RUTHERFORD EXPERIMENT: ENERGY DIPENDECE

We acquired data by keeping constant the angle between the beam direction and the detector at  $160^\circ$ , and by varying the alpha beam energy  $E$  (Table 1). The target we used was a thin gold on silicon layer. We analysed the dependence between  $1/E^2$  and the cross section, to achieve a linear graphic (Figure 1). One of the obtained histograms is shown in Figure 2 in the case of an  $\alpha$  beam energy of 2 MeV and fixed scattered angle of  $160^\circ$ . The cross section is proportional to a measurable variable, called normalized counts. We counted the backscattered alpha particles, and we normalized them to the charge. The charge  $Q$  can be obtained by multiplying the intensity of the beam  $I$  in nA and the data taking period  $t$  in s.

Table 1: Normalized counts as a function of  $\alpha$ -beam energy at fixed scattered angle of  $160^\circ$ .

Normalized counts		
Energy (MeV)	(1/ $\mu$ C)	$\frac{1}{E^2} (\frac{1}{MeV^2})$
1,2	11655	0,69
1,3	9691	0,59
1,4	8564	0,51
1,5	7550	0,44
1,6	6775	0,39
1,7	5938	0,35
1,8	5300	0,31
1,8	5308	0,31
1,9	4715	0,28
2,0	4328	0,25
2,0	4278	0,25

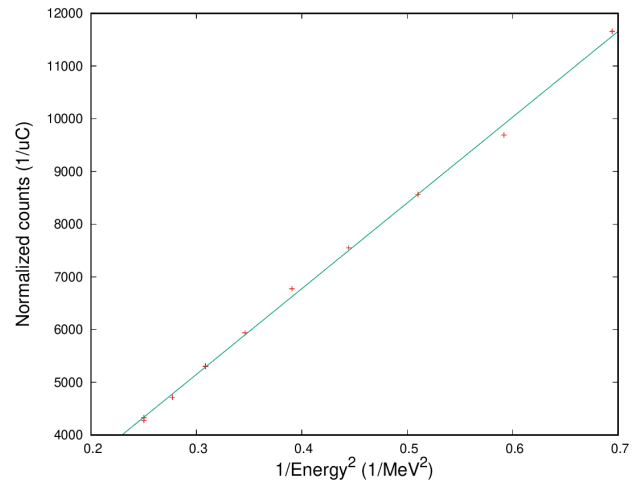


Figure 1: Plot of normalized counts as a function of  $\alpha$ -beam energy at fixed scattered angle of  $160^\circ$ . The fitted  $F(x) = Ax + B$  with parameters  $A = 16300 \text{ MeV}^2/\mu\text{C}$ ,  $B = 270 \text{ 1}/\mu\text{C}$  is overlaid with the data.

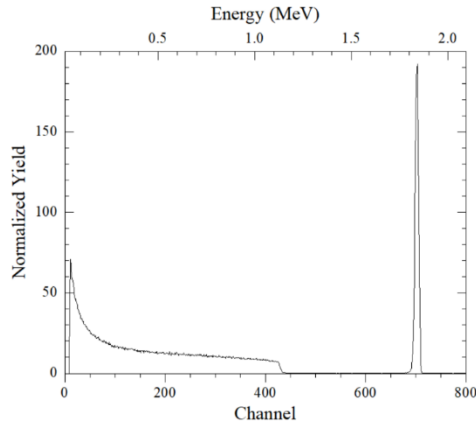


Figure 2: Energy spectrum of a gold on silicon target at a beam energy of 2 MeV and fixed scattered angle of 160°. A clear peak in energy is present at 1.84 MeV.

### RUTHERFORD EXPERIMENT: ANGLE DIPENDECE

We acquired data by keeping constant the alpha beam energy, and by varying the angle to analyse the relationship between the scattering angle ( $\theta$ ) of the  $\alpha$  particle and the cross section. In this measurement the constant beam energy was at 1.8 MeV and the target was composed of a layer of gold on silicon.

On the x axis we set a range of angles from 100 to 170 degrees because our detector was placed at backward angles, since we are exploiting the Rutherford Backscattering technique.

Figure 3 shows the data and the following formula:  $\frac{1}{\sin^4(\frac{\theta}{2})}$ . When  $\theta$  increases, the cross section decreases and the data follow correctly the trend of the curve. In Table 2 we can see normalized counts as a function of scattered angle with  $\alpha$ -beam energy fixed at 1.8 MeV.

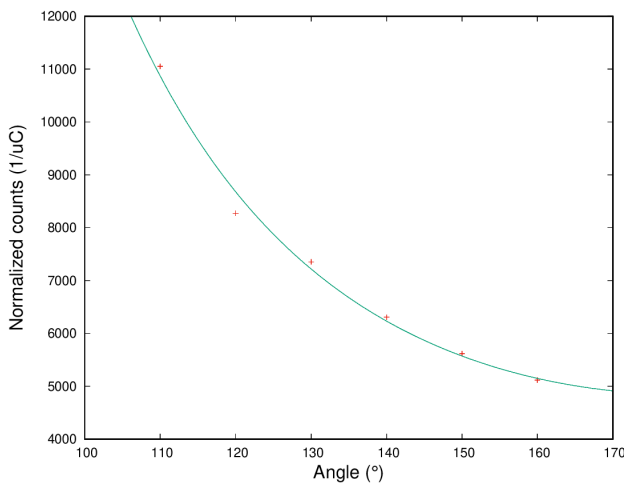


Figure 3: Normalized counts as a function of the scattering angle with a beam energy of 1.8 MeV. The fitted  $F(x) = \frac{A}{\sin^4(\frac{\theta}{2} + B)}$  with parameters  $A = 4900$  1/μC,  $B = 99$  is overlaid with the data.

Table 2: Normalized counts as a function of scattered angle with  $\alpha$ -beam energy fixed at 1.8 MeV.

Scattering Angle (°)	Normalized counts (1/μC)
160	5117
150	5620
140	6307
130	7352
120	8272
110	11052

### RUTHERFORD EXPERIMENT: STUDY OF MATERIALS

We have collected data from 6 different targets with a fixed angle of 160° and fixed  $\alpha$  beam energy of 1.8 MeV.

The position of the centroid depends on the atomic mass and the thickness of the target (Figure 4). Heavier atoms absorb more energy, while lighter atoms absorb less energy.

The material's thickness difference, in the order of nanometers, causes a variation on the peak's width on the x axis, as we can see in Figures 5 and 6.

We have used then the RBS technique to analyze the chemical composition of an unknown material. The graph shows the main curve starting at Channel 400, which indicates the presence of Si, and a small peak near channel 250. This peak must be caused by a lighter element than Si. With further investigation we concluded that it was a target of SiO<sub>2</sub> on Si (Figure 7.)

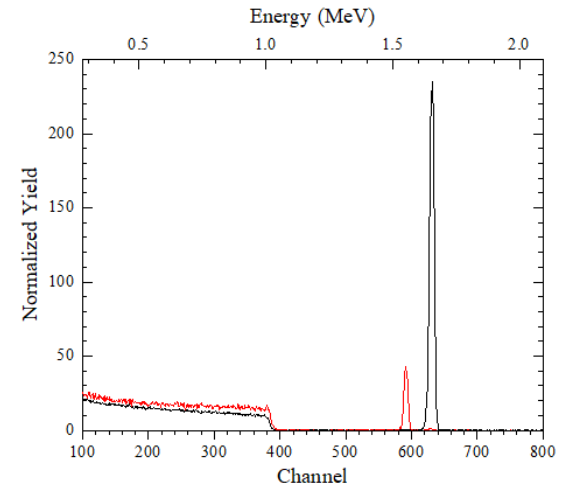


Figure 4: Plot of target Z=46 (Pd) on Z=14 (Si) (in red) compared to a target Z=79 (Au) on Z=14 (Si) (in black) at fixed  $\alpha$  beam energy of 1.8 MeV and fixed scattered angle of 160°.

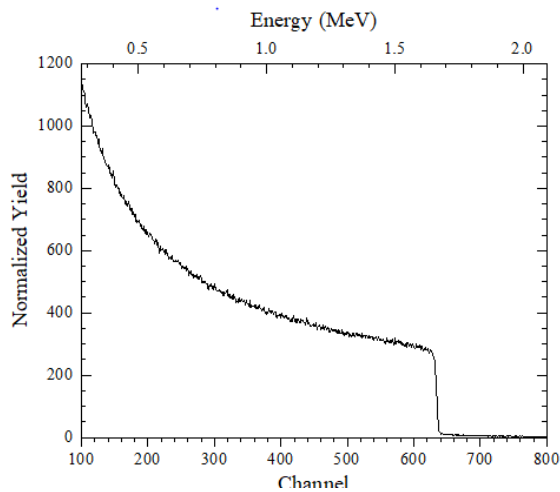


Figure 5: Pure Gold. Plot of target  $Z=79$  (Au) (in black) at fixed a beam energy of 1.8 MeV and fixed scattered angle of  $160^\circ$ .

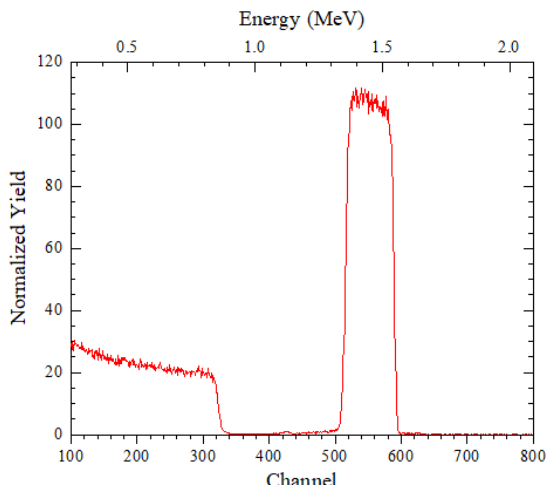


Figure 6: Ruthenium on silicon. Plot of target  $Z=44$  (Ru) on  $Z=14$  (Si) at fixed a beam energy of 1.8 MeV and fixed scattered angle of  $160^\circ$ .

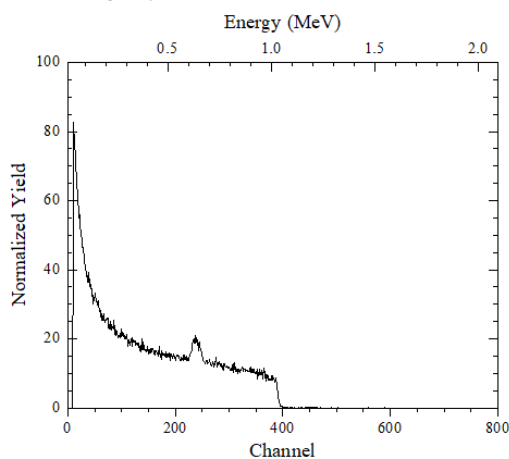
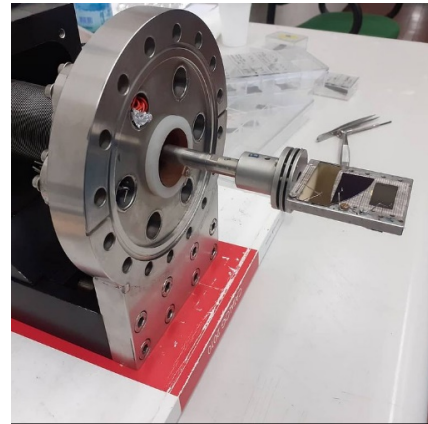


Figure 7: Silica ( $\text{SiO}_2$ ) on silicon. Plot of target Si at fixed a beam energy of 1.8 MeV and fixed scattered angle of  $160^\circ$ .

## ACCELERATOR AN2000

The AN2000 [2] is an electrostatic accelerator with a maximum voltage terminal of 2MV. It is able to accelerate protons or alpha particles (He) with +1 charge. The main usage is to analyse materials to unveil their chemical composition and the distribution profiles of the constituent elements. It was installed in the Legnaro National facility of INFN in 1971.

Figure 8: View of targets on the holder.



## ELECTRONICS, DATA ACQUISITIONS AND STORAGE

In the experiment we used a silicon detector located at 7 cm of distance from the target, powered by an electric field of +60V. The area of the detector is  $25 \text{ mm}^2$ , the solid angle covered by the detector is 0.0051 sr. The resolution of the electronic chain [3] is 3 keV as verified with the signal of a pulser.

The experimental system is composed by a preamplifier situated nearby the detector, to amplify only the signal and not the noise. After the data collection, we analysed the noise and we found out that it did not affect the result of the experiment. After the preamplifier, there is the amplifier, whose role is to amplify and generate the signal for the analogic to digital converter (ADC). The dynamic range of the ADC is 11 (0;2047). A dedicated charge integrator gives the quantity  $Q$  used for normalization. In the electronic crate we have also a pulser and a master module.

The data acquisition system is a state machine. The state we used are start, stop, reset, and save. The data acquisition system is safe, comfortable, and user-friendly.

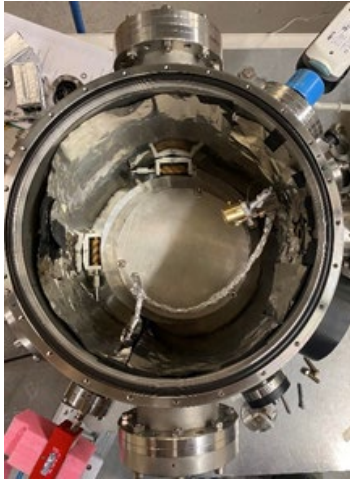
We collected the data in a logbook and we used about 50 kB of memory for the data files, which have the .rbs extension and were saved with a self describing name such as:

"21\_6\_16\_EBS\_alfa\_Au\_Si\_n1\_1200keV\_20g\_ch\_42 69.rbs".



The software used for data analysis consists in various programs: Xrump version 9.095, Gnuplot version 5.4, Excel and Root version 6.12, based on C++.

Figure 9: Preamplifier near the reaction chamber



### CONCLUSIONS

Our data are in good agreement with the Rutherford formula:

$$\frac{d\sigma}{d\Omega} = \left(\frac{\alpha}{4E}\right)^2 \frac{1}{\sin^4 \frac{\theta}{2}}$$

We also were able to recognise unknown target materials by using the Rutherford backscattering technique. We verified that different materials return different responses of the energy spectra.

### ACKNOWLEDGEMENTS

We thank AN2000 accelerator staff, Leonardo La Torre and Davide Carlucci and the beam coordinator Valentino Rigato. It was a pleasure to work with Matteo Campostrini, who allowed us to study on these targets.

Figure 10: The experimental group.



---

### REFERENCES

- [1] Rutherford, E 'LXXIX. The scattering of  $\alpha$  and  $\beta$  particles by matter and the structure of the atom', Philosophical Magazine Series 6, 21: 125, (1911) 669 – 688
- [2] INFN, AN2000, <http://www.lnl.infn.it/index.php/en/accelerators-3/an-2000>
- [3] Manual ORTEC, Model 710 quad 1-kV Bias Supply Operating and Service Manual, ORTEC® Part No. 761850 Manual Revision F

# Making Of a Heat Sink: Illustration, Heat Dissipation, Design, and Work Cycle

F. Montanari<sup>1</sup>, G. Vendrame<sup>2</sup>

<sup>1</sup> LS Volta Fellini di Riccione, (Rimini), Italy

<sup>1</sup> IIS Duca degli Abruzzi di Treviso, (Treviso), Italy

## INTRODUCTION

We have designed and then manufactured a heat sink with the use of machine-tools.

Starting from an idea, we then moved on to the physical study of the object and the digital drawing, then to the choice of the raw piece and the design of the work cycle. Finally, we moved on to the making of the finished product from the solid through a lathe machining.

## RUTHERFORD EXPERIMENT: ENERGY DIPENDECE

When thermal machines heat up, they must be cooled down to avoid malfunctions. This heat in fact must be dissipated so that the system does not have an excessive temperature. To decrease the thermal resistance of a device/system we therefore need to cool it. One solution is to physically connect the system to a device called a heat sink. It is a metal device shaped to provide a large surface area and facilitate heat dissipation.

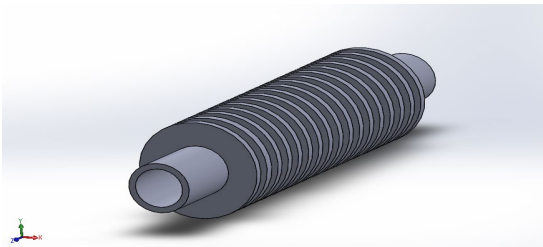


Figure 1: 3D model of our hollow cylindrical heatsink with 17 circular dissipation fins.

## HEAT SINK: THERMAL CONDUCTIVITY

To design an efficient heat sink, we have used Fourier's postulate. This allows to determine the thermal power exchanged by a solid object, hence the heat dissipated per unit time.

$$P = -\lambda \cdot A \cdot \frac{\Delta T}{\Delta x}$$

- $P$  = the thermal power exchanged (W);
- $\lambda$  = coefficient of conductivity (depends on the material);
- $A$  = the area of the section of the plate (m<sup>2</sup>);
- $\frac{\Delta T}{\Delta x}$  = the thermal gradient, which is the temperature variation with respect to the thickness (K/m).

During the design phase we dealt with the surface area and thickness parameters.

By creating many circular dissipation fins of large diameter, the surface will increase, so will the dissipation ability of the device.

Whereas in the phase of choice of material, we focused on the coefficient of conductivity of the different materials.

## IDEA AND DESIGN

We started with a physical study of a fluid heat sink and made a hand sketch using standard measurements.

In the design phase on SolidWorks® the measurements of the total area have been increased to obtain a greater dissipation. SolidWorks® is a three-dimensional parametric design and drafting software dedicated to mechanical engineering.

After having designed the product in 3D, we made the title block with all the necessary dimensions, tolerances, and various projections.



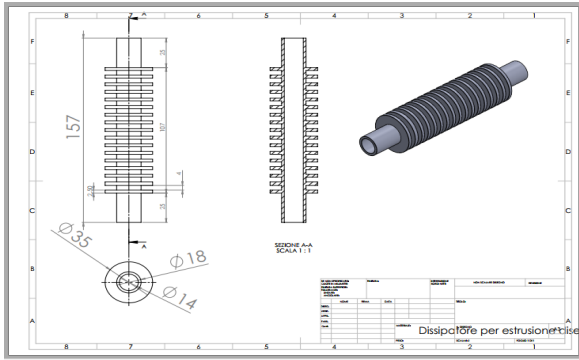


Figure 2: the heat sink design drawn in Solidworks.

## MATERIAL AND BLANK SELECTION

Then we were able to go to the warehouse for the selection of the material.

For the making of a product, we must consider the material resources and skills and the quality of the product. In addition, we had to choose an appropriate black to reduce the margins of error within acceptable levels and the waste of material and time.

Aluminum and copper are the most suitable in the production of heat sinks due to their high thermal conductivity.

<b>Steel Cr 20%:</b>	<b>22</b>
<b>Steel Cr 1%:</b>	<b>61</b>
<b>Iron:</b>	<b>73</b>
<b>Aluminum:</b>	<b>204</b>
<b>Copper:</b>	<b>386</b>
<b>Silver:</b>	<b>407</b>

Table 1: The coefficient  $k[W/m^{\circ}C]$  for some materials, at the temperature of  $25^{\circ}C$ .

Aluminum is the most widely used metal for making heat sinks, but sometimes copper is also used. We have

examined several evaluation criteria to discover the qualities and defects of the two materials. Copper is thermally more conductive than aluminum, as the table above attests. Our choice, however, has fallen on aluminum, since with this you will get a heat sink with greater strength and lightness.

The raw piece chosen was a solid bar of 6082 Anticorodal aluminum of diameter 40mm and length 160mm, which are dimensions close enough near to the ones of our final piece.

The general characteristics of this aluminum-silicon-magnesium-manganese alloy include good strength values, good corrosion resistance, and good machinability.

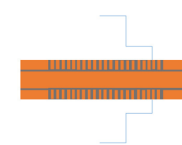


Figure 3: Materials and selected bar.

## WORKING CYCLE AND MAKING PROCESSES

After choosing the workpiece, the work cycle is elaborated to arrive at the final making, also choosing the various tools (for facing, removing, drilling, countersinking, beveling, etc.).

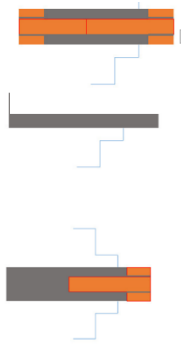
We positioned the workpiece in the self-centering spindle of the lathe at 40 mm from the face.



PROCESSES	TOOL USED
1) Facing	External turning tool
2) Turning until a diameter of 18mm	External turning tool
3) Centering	Bit for centering
4) Drilling a dia 11.5mm, 80mm depth	Drilling tool (11mm bit)
5) Drilling dia 14mm	Drilling tool (14mm bit)
6) Countersinking of the internal hole	Countersink
7) Beveling of the external diameter	Beveling tool placed at $45^{\circ}$

The last tool has an insert coated with a deposit of titanium nitride, The deposit, made by sputtering, increases the strength and durability of the tool.

Afterwards we positioned the workpiece in the spindle from the opposite side.

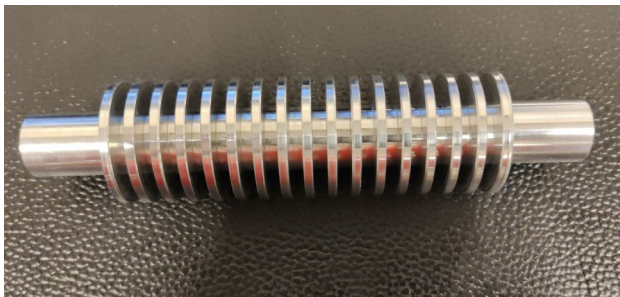
	PROCESSES	TOOL USED
	1) Facing bringing the piece to 157mm	External turning tool
	2) Turning until a diameter of 18mm	External turning tool
	3) Centering	Bit for centering
	4) Drilling a dia 11.5mm, 80mm depth	Drilling tool (11mm bit)
	5) Drilling dia 14mm	Drilling tool (14mm bit)
	6) Countersinking of the internal hole	Countersink
	7) Beveling of the external diameter	Beveling tool placed at 45°

We then locked the spindle at 5 mm from the face.

PROCESSES	TOOL USED
1) Turning until a diameter of 35mm	External turning tool
2) Making grooves	Grooving tool
3) Beveling of the fins	Beveling tool placed at 45°



Eventually, we performed the machining operations listed in the work cycle in order.



## ACKNOWLEDGEMENTS

Through this experience we have increased our knowledge and practical skills related to mechanics. Special thanks go to our tutors Alessandro Minarello, Flavio Pasquato, Alex Battistello, Diego Giora, who helped us conduct the research, the subject of the paper, at the company.



# Study of the sputtering yield for the production of negative ion beams for the Tandem accelerator of LNL

A. Ballarini<sup>1</sup>, A. Gomiero<sup>2</sup>

<sup>1</sup>*I.I.S.P. Scatcerle di Padova, (Padova), Italy*

<sup>2</sup>*I.T.T.G. Marconi di Padova, (Padova), Italy*

## INTRODUCTION

In this scientific article we will show a series of tricks and methods to increase the sputtering yield involved in the formation of a negative ion beam for the Tandem accelerator.

## PARTICLE ACCELERATORS

A particle accelerator is a machine whose purpose is to deliver beams of charged ions or subatomic particles, including electrons, positrons, protons, and antiprotons, and then made to collide with each other at high kinetic energy.

The methods for accelerating particles are based on the joint use of electric and magnetic fields: the former provide energy to the charged particles by accelerating them, while the latter eventually serve to bend their trajectory by exploiting the Lorentz force or to counteract the natural beam divergence.

These machines are mainly used for industrial (60%) purposes (for example, ion implantation), medical (35%) (for example, for the production of radioactive isotopes), study of the structure of materials or for research purposes (5%) in particle and nuclear physics.

## OPERATION OF A SPUTTERING SOURCE FOR PARTICLE ACCELERATORS

One of the most used methods to produce the negative ion beams for accelerators involves the sputtering process (collision of ions with the sample to be ionized). It takes place inside the accelerator source which is formed by a set of metal components that enclose a chamber in which it is possible to create a vacuum.

The sample from which the ions to be accelerated must be obtained is placed in a copper cylinder which is connected to a metal rod (sputtering rod). The rod with the sample is inserted inside the source which is sealed to create a vacuum. Cesium (a liquid alkaline metal at room temperature) is inserted through a lateral tube at the source, which is heated and evaporated by means of a resistance.

The cesium, in the form of vapor, is conveyed into the chamber through a metal tube and can touch the ionizer (a spherical electrode at a temperature of about 1200 ° C): therefore, it is ionized through surface ionization (it loses an

electron and becomes positively charged). The cesium cation is subsequently accelerated towards the copper cone (which has been negatively biased with respect to the ionizer) containing the sample, causing its atoms to escape from the copper cone.

In positive ion accelerators (such as those present at the National Laboratories of Nuclear Physics in Legnaro) the beam of negative ions, after being accelerated by a potential difference, is made to impact against one or more thin sheets of carbon. The carbon in the sheet strips one or more electrons from the sample anions making them positively charged.

## YIELD OF THE SPUTTERING PROCESS

The sputtering process, through which the ion beam to be accelerated is formed, has an efficiency (sputtering yield) which is calculated using the following formula:

$$\text{Sputtering yield} = \frac{\text{Spattered Atoms}}{\text{Impacted Ions}}$$

The sputtering yield is therefore obtained by dividing the number of atoms in the sample that have detached from it by the number of ions that have caused them to escape. It depends on:

- Impacting ion beam energy
- Angle of incidence of the impacting ion beam
- Sample thickness
- Type of impacting ion

All these aspects will be analyzed in the following sections.

## IMPACTING ION BEAM ENERGY

Using the S.R.I.M (the Stopping and Range of Ions in Matter) software we have created sputtering simulations by varying in each of the simulations only the energy of the impacting ions.

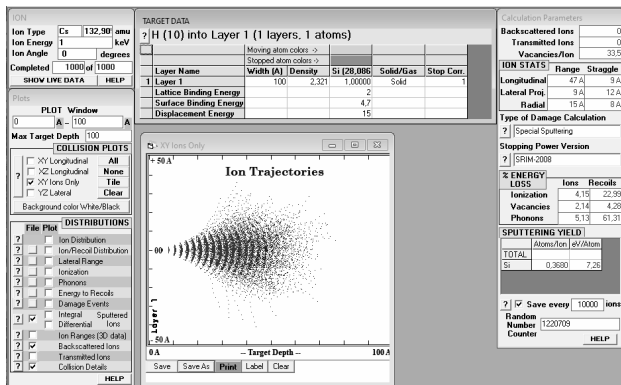


Figure1 Simulation of the perpendicular impact of a 1 KeV cesium ion beam on a sample layer with a thickness of 100 Å.

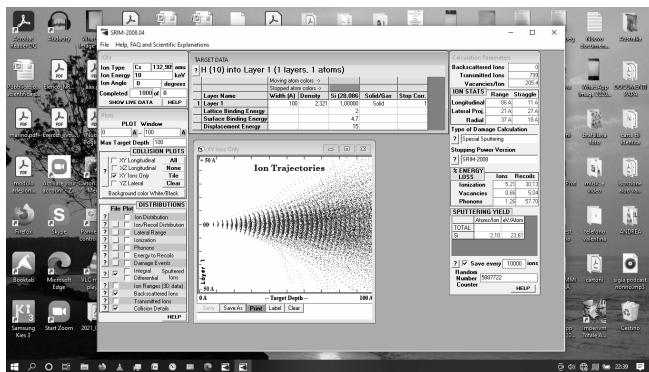


Figure2 Simulation of the perpendicular impact of a 10 KeV Cesium ion beam on a sample layer with a thickness of 100 Å.

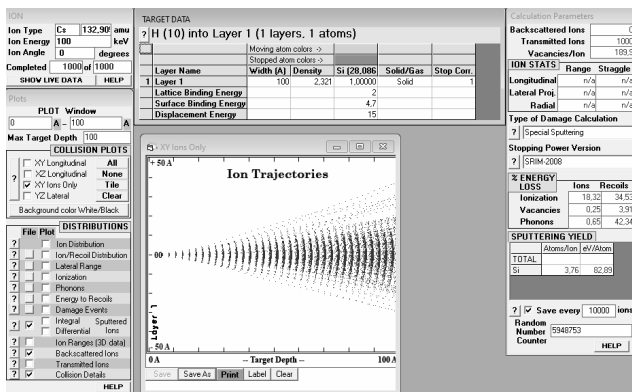


Figure3 Simulation of the perpendicular impact of a 100 KeV Cesium ion beam on a sample layer with a thickness of 100 Å.

Table1 First simulation data.

IMPACTING ION	ACCIDENT BEAM ENERGY (keV)	ANGLE OF INCIDENCE (°)	SAMPLE	SAMPLE THICKNESS (Å)	SPUTTERING YIELD
Cesium	1	0	Silicon	100	0,368
Cesium	10	0	Silicon	100	2,100
Cesium	100	0	Silicon	100	3,760

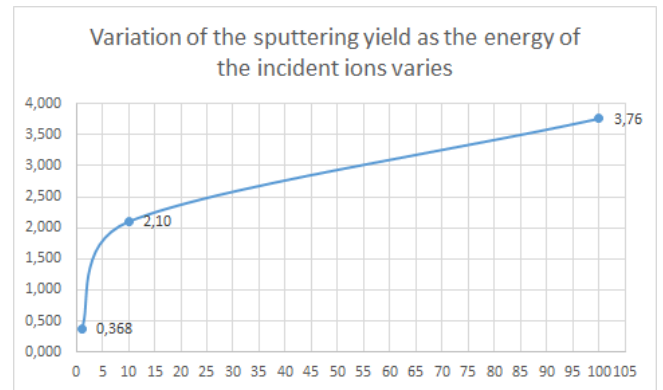


Figure4 Variation of the sputtering yield as a function of the incident energy Impacting ion: Cesium, Sample: Silicon

From the results of the simulations, it can be clearly observed that a greater energy (and therefore a greater speed) of the ions impacting the sample results in a considerable increase in the yield of the sputtering process.

This phenomenon can be explained by the fact that a greater energy of the impacting particles causes much stronger collisions and therefore a greater transfer of kinetic energy to the particles of the sample which consequently can escape in a greater number.

To increase the energy of the impacting ion beam, we act on the potential difference between the copper cone containing the sample. This would lead to an increase in the speed of the impacting ions (attracted by the potential difference). This expedient would consequently and significantly increase the yield of the sputtering process.

## ANGLE OF INCIDENCE OF THE IMPACTING ION BEAM

Again, using the S.R.I.M (the Stopping and Range of Ions in Matter) software, we carried out sputtering simulations by varying only the angle of incidence of the impacting ion beam.

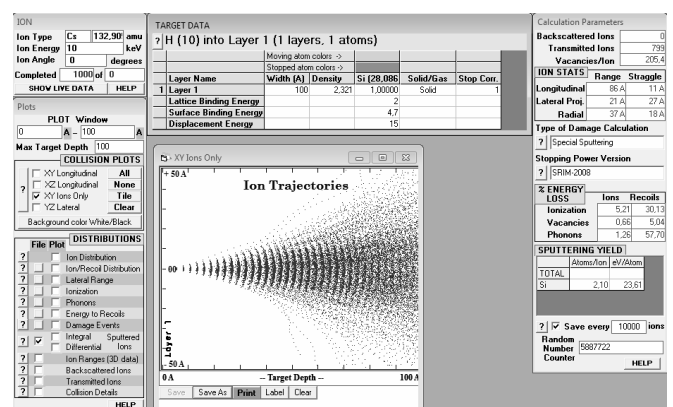


Figure5 Simulation of the perpendicular impact of a 10 KeV Cesium ion beam on a sample layer with a thickness of 100 Å.

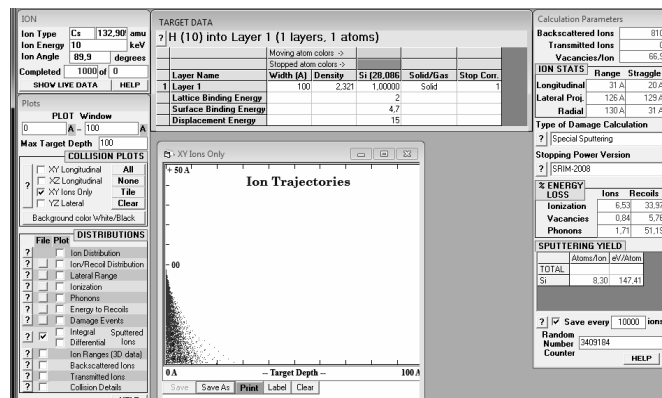
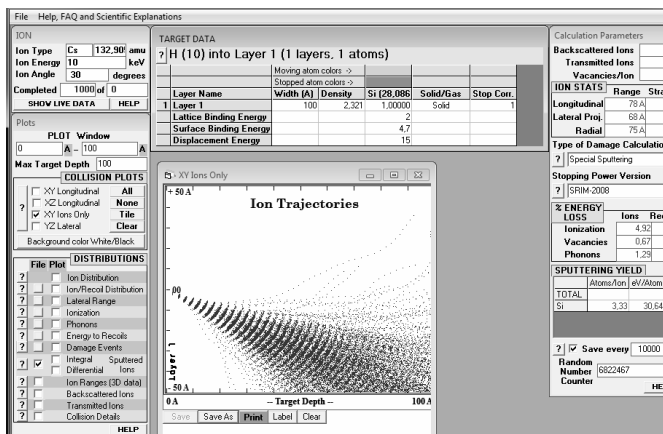


Figure9 Simulation of the impact with an incidence angle of 89.9 ° of a beam of Cesium ions at 10 KeV on a sample layer with a thickness of 100 Å.

Figure6 Simulation of the impact with an incidence angle of 30 ° of a beam of Cesium ions at 10 KeV on a sample layer with a thickness of 100 Å.

Table2 Second simulation data

IMPACTING ION	ACCIDENT BEAM ENERGY (KeV)	ANGLE OF INCIDENCE (°)	SAMPLE	SAMPLE THICKNESS (Å)	SPUTTERING YIELD
Cesium	10	0	Silicon	100	2,100
Cesium	10	30	Silicon	100	3,330
Cesium	10	60	Silicon	100	11,930
Cesium	10	70	Silicon	100	19,120
Cesium	10	89,9	Silicon	100	8,300

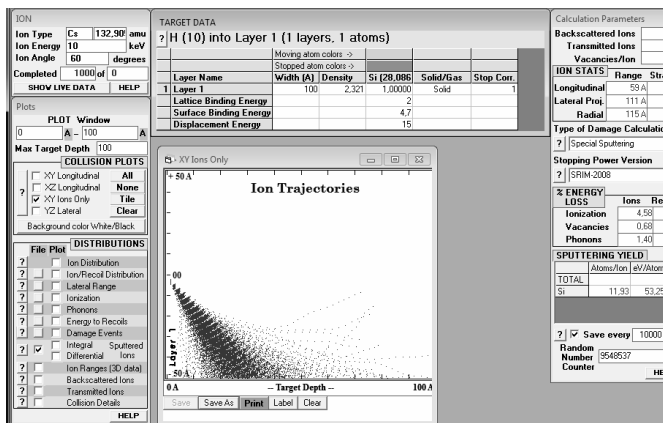


Figure7 Simulation of the impact with an incidence angle of 60 ° of a beam of Cesium ions at 10 KeV on a sample layer with a thickness of 100 Å.

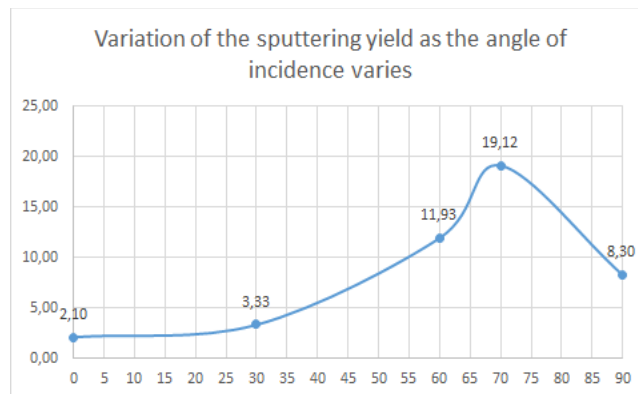


Figure10 Variation of the sputtering yield as a function of the incidence angle

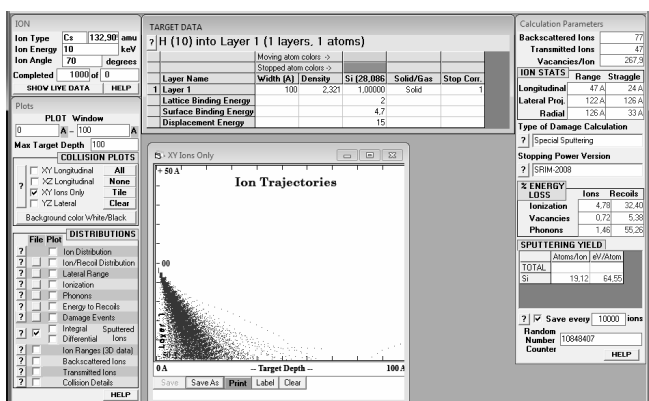


Figure8 Simulation of the impact with an incidence angle of 70 ° of a beam of Cesium ions at 10 KeV on a sample layer with a thickness of 100 Å.

This phenomenon can be explained by the fact that at smaller angles the impacting particles are unable to maximize the expulsion of sample particles.



To vary the angle of incidence of the ion beam, the output of the ion beam could be positioned laterally with respect to the copper cone. This would lead to an increase in the angle of incidence (to be kept within the limit of 70 °) of the ions on the sample and therefore an increase in the sputtering yield would result.

SAMPLE THICKNESS

Again, using the S.R.I.M (the Stopping and Range of Ions in Matter) software, we created sputtering simulations by varying only the thickness of the sample in each of the simulations.

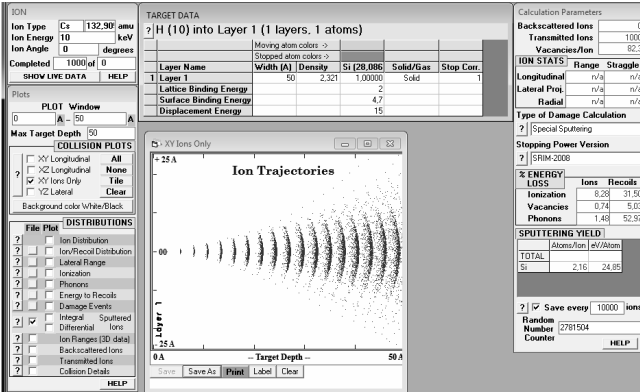


Figure11 Simulation of the perpendicular impact of a 10 KeV cesium ion beam on a sample layer with a thickness of 50 Å.

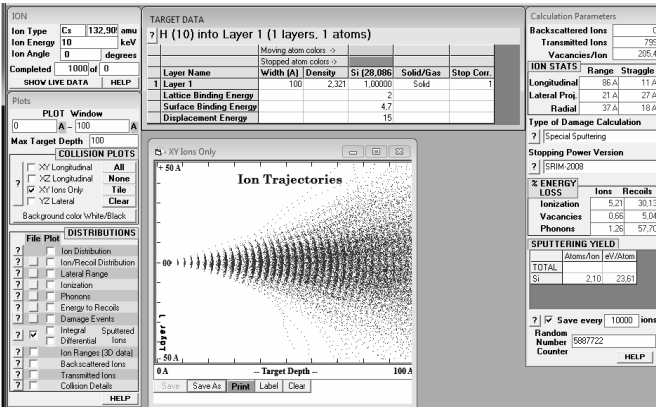


Figure12 Simulation of the perpendicular impact of a 10 KeV Cesium ion beam on a sample layer with a thickness of 100 Å.

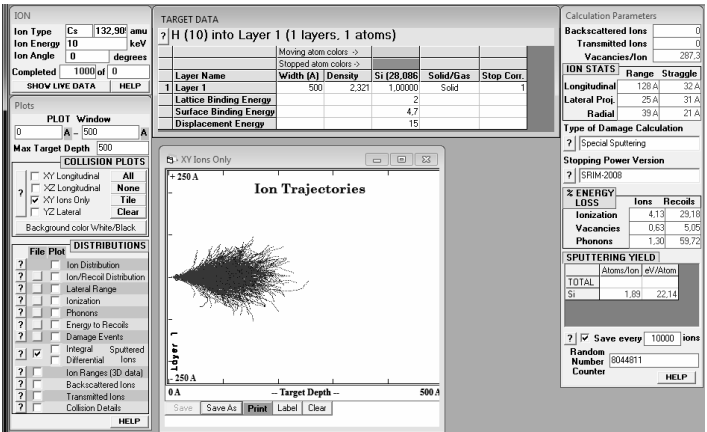


Figure13 Simulation of the perpendicular impact of a 10 KeV cesium ion beam on a sample layer with a thickness of 500 Å.

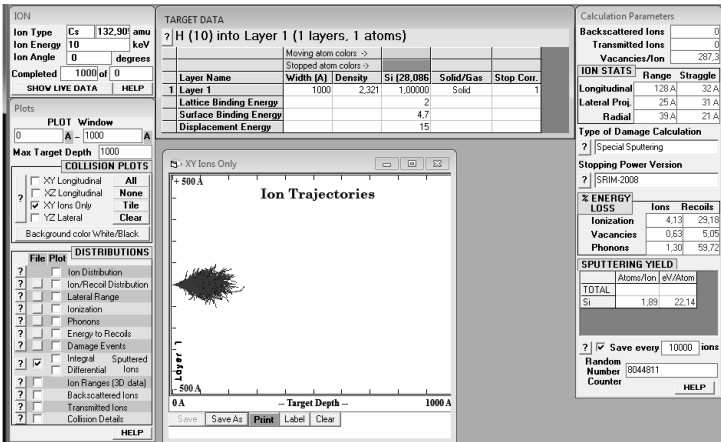


Figure14 Simulation of the perpendicular impact of a 10 KeV Cesium ion beam on a sample layer with a thickness of 1000 Å.

Table3 Third simulation data

IMPACTING ION	ACCIDENT BEAM ENERGY (KeV)	ANGLE OF INCIDENCE (°)	SAMPLE	SAMPLE THICKNESS (Å)	SPUTTERING YIELD
Cesium	10	0	Silicon	10	1,26
Cesium	10	0	Silicon	50	2,16
Cesium	10	0	Silicon	100	2,10
Cesium	10	0	Silicon	500	1,89
Cesium	10	0	Silicon	1000	1,89

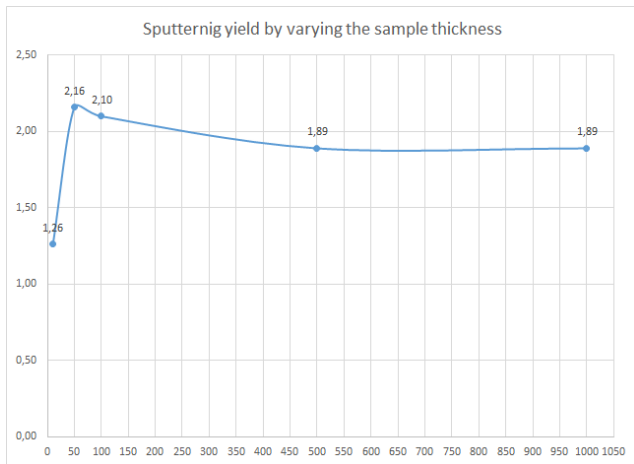


Figure15 Sputtering yield by varying the sample thickness.

From the results of the simulations, it can be clearly observed how a higher thickness of the sample translates into a higher sputtering yield (up to a thickness of about 50 Å).

This phenomenon can be explained by the fact that the more the thickness of the sample increases (within 50 Å) the greater is the number of atoms in the sample available to be impacted by the cesium ions. This results in a higher sputtering yield.

When the sample thickness increases beyond 50 Å it can be seen how the sputtering yield gradually decreases.

This phenomenon can be explained by the fact that the more the thickness of the sample increases (over 50 Å), the more the particles inside it, at the same angle and energy absorbed in the impact are more disadvantaged in crossing the greater number of layers of the sample. to exit. This results in a lower sputtering yield.

Therefore, to increase the sputtering yield, it would be sufficient to deposit the thinnest layers of the sample to be used on the copper cone (around the maximum yield 50 Å).

## TYPE OF IMPACTING ION

Again, using the S.R.I.M (the Stopping and Range of Ions in Matter) software, we created sputtering simulations by varying in each of the simulations only the type of ion used for the impact on the sample.

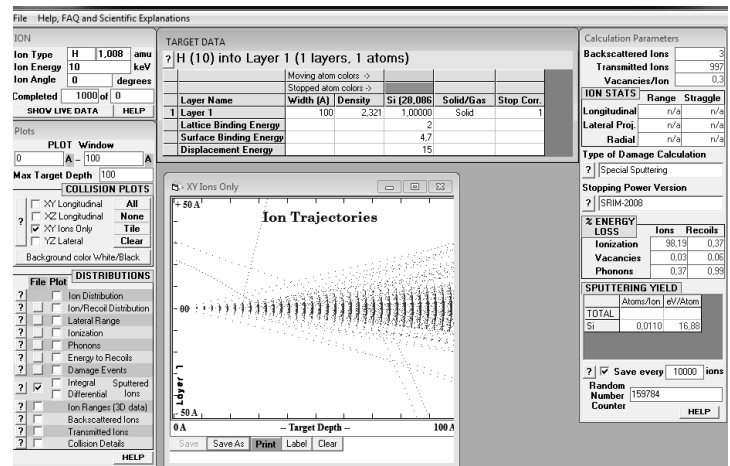


Figure16 Simulation of the perpendicular impact of a beam of protons ( $H^+$ ) at 10 KeV on a sample layer with a thickness of 100 Å.

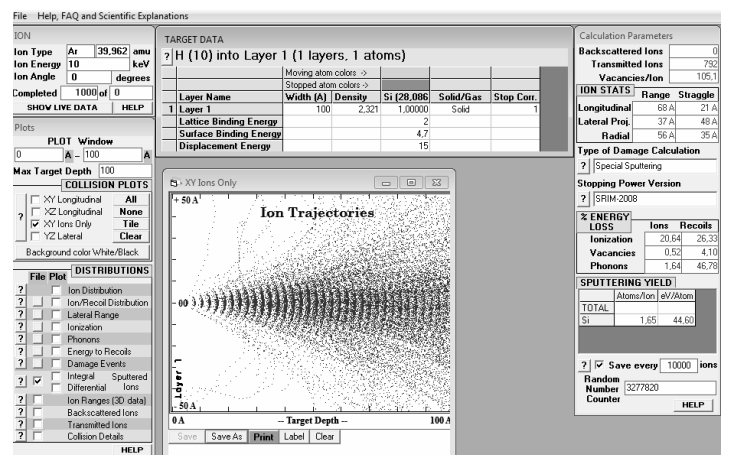


Figure17 Simulation of the perpendicular impact of an Argon ion beam at 10 KeV on a sample layer with a thickness of 100 Å.

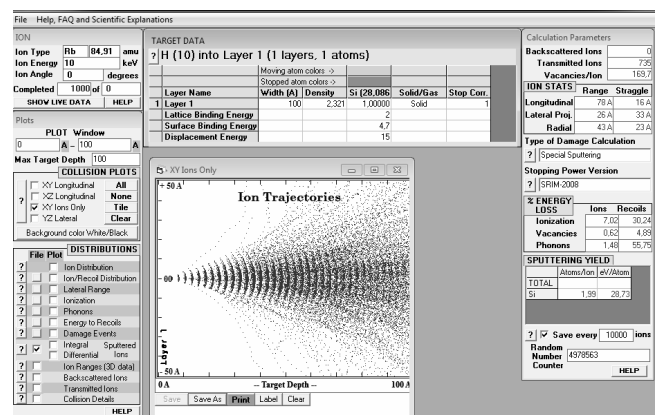


Figure18 Simulation of the perpendicular impact of a 10 KeV Rubidium ion beam on a sample layer with a thickness of 100 Å.

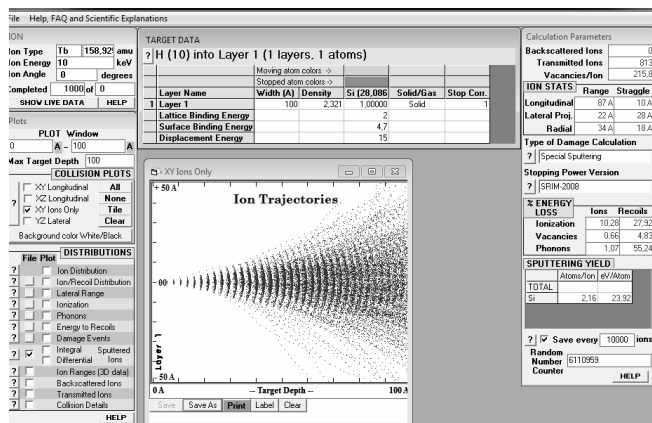


Figure19 Simulation of the perpendicular impact of a 10 KeV Terbium ion beam on a sample layer with a thickness of 100 Å.

Table4 Fourth simulation data

IMPACTING ION (Z)	ACCIDENT BEAN ENERGY(Ke V)	ANGLE OF INCIDENT CE (°)	SAMPLE	SAMPLE THICKNESS (Å)	SPUTTERING YIELD
Hydrogen (1)	10	0	Silicon	10	0,011
Argon (18)	10	0	Silicon	50	1,65
Rubidium (37)	10	0	Silicon	100	1,99
Terbium (65)	10	0	Silicon	500	2,16

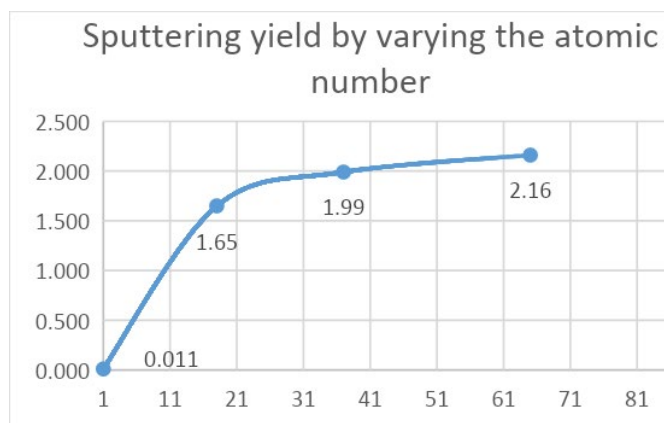


Figure20 Sputtering yield by varying the atomic number.

From the results of the simulations, it can be clearly observed that an increase in the atomic radius corresponds to an increase in the sputtering yield.

This phenomenon can be explained by the fact that the more the atomic radius of the impacting ions increases, the more they interact with the atoms of the sample, leading to a greater leakage from the sample and consequently a greater sputtering yield.

Therefore, using elements with an atomic radius greater than cesium as ions to be impacted would result in a greater yield of the sputtering process.

## CONCLUSIONS

Through computer simulations with the S.R.I.M software we have conclude that there are four ways to significantly increase the yield of the sputtering process. To put these solutions into practice, the ion sources of the accelerators could therefore be modified, or the chemical species used to produce the ion beam could be varied.

Theoretically the maximum yield is obtained with an angle of 70 °, with a uranium bullet and using the maximum applicable voltage and a sample thickness of 50 Å.

# Physics Applied To Cultural Heritage

G. Dal Maso<sup>1</sup>, F. Di Fazio<sup>2</sup>, E. Gomiero<sup>3</sup>

<sup>1</sup>Liceo Statale A.M. Roveggio - G. Veronese, Cologna Veneta (VR), Italy

<sup>2</sup>Liceo Statale V. Alfieri, Asti (AT), Italy

<sup>3</sup>Liceo Statale G. Galilei, Selvazzano Dentro (PD), Italy

## INTRODUCTION

The inspection of a work of art is without any doubt a very important issue for conservators and art historians as it allows to identify the materials and the pigments used. In addition, it helps experts of history and art to define the artist's technique, to trace the production and the story of the work. It also is very helpful to conservators when it comes to the restoration process.

Each one of the techniques described in this article can make experts of history and art aware of all the issues summarized above. Moreover, they are all non-destructive and non-invasive techniques: thanks to this, the artwork is not likely to report any sign of damage during the process of analysis.

## MATERIALS AND METHODS

We analyzed pigments, a post-byzantine icon, jewels, and rocks. We considered the methods: false color photography by means of infrared (IR) and ultraviolet (UV) light, XRF spectroscopy, PIXE technique and Raman spectroscopy, radiography, and tomography. The pigments analyzed were standards from *Kremer GMBH*, namely:

- **MANGANESE BLACK** (47500)  
 $\text{MnO}_2$
- **TITANIUM WHITE** (46200)  
 $\text{TiO}_2$
- **PRUSSIAN BLUE** (45200)  
 $\text{FeK}[\text{Fe}(\text{CN})_6]$
- **COBALT YELLOW** (43500)  
 $[\text{Co}(\text{NO}_2)_6]\text{K}_3 + 3\text{H}_2\text{O}$
- **ALIZARINE CRIMSON DARK** (23610)  
 $\text{C}_{14}\text{H}_8\text{O}_4$
- **AZURITE** (10201)  
 $\text{Cu}_3(\text{CO}_3)_2(\text{OH})_2$
- **CAPUT MORTUUM** (48700)  
 $\text{Fe}_2\text{O}_3$
- **INDIAN YELLOW** (23350)  
 $\text{C}_{19}\text{H}_{16}\text{MgO}_{11} \cdot 6\text{H}_2\text{O}$
- **TERRA ERCOLANO** (41600)

$\text{Fe}_2\text{O}_3$

- **AEGIRINE** (11140)  
 $\text{NaFeSi}_2\text{O}_6$
- **BLUTSTEIN** (48651)  
 $\text{Fe}_2\text{O}_3$
- **INDIGO** (36005)  
 $\text{C}_{16}\text{H}_{10}\text{N}_2\text{O}_2$
- **CINNABAR** (10620)  
 $\text{HgS}$

## INFRARED AND ULTRAVIOLET PHOTOGRAPHY

Prior to the analysis the conservation status of an artwork should be documented by photographic campaigns under visible infrared and ultraviolet light. IR light can enlighten tonalities while UV puts in evidence previous restorations and interventions. Both IR and UV photography can be performed in normal and false color modes. The aim of the false color technique is to visually discriminate different pigments. This technique is based on overlapping two different photographs: the first one is taken in the visible part of the electromagnetic spectrum while the second one is in the infrared domain. Afterwards the visible picture is divided into the RGB components (red, green, blue) while the infrared one is translated into a grayscale. The last step consists in modifying these channels by moving the infrared picture on the red channel, the red component on the green channel, the green component on the blue channel and not considering the blue component. For the analysis we used a Samsung NX3300 mirrorless modified camera, provided with two visible-light and infrared-light stopping filters. On infrared false color some pigments like cinnabar and indigo change color and lead to an immediate identification without any color inspection. In Figure 1, visible infrared and false color images of the pigments are reported. From the picture it is evident that the cinnabar changes from red to bright yellow while indigo changes from dark blue to red. Figure 2 reports infrared false color and ultraviolet false color of the post-byzantine icon. The

UV allows to identify the region of the previous restoration on the right side of the icon.



Figure 1: visible, infrared, and false color of the thirteen Kremer pigments analyzed.



Figure 2: A comparison between the original icon (on the right side), its photos using IR and UV lights (on the left side) and their respective false color pictures (in the middle).

## XRF SPECTROSCOPY

XRF (X-Ray Fluorescence) is used to determine the elemental composition of the analysis materials. XRF technique can detect elements from sodium (Na;  $Z=11$ ) to uranium (U;  $Z=92$ ). A beam of electrons is emitted to hit a tungsten foil (anode). Then, X-rays are emitted from tungsten and sent to impinge on the material. Once hit, the material emits X-rays with defined energy. All these energies are elaborated by a terminal, which enables researchers to see the spectrum of the various elements composing the sample. Thanks to the spectrum, it is possible to find the quantity of each element in the material.

The XRF analysis was performed by means of a LITHOS3000 (ASSING) portable XRF spectrometer. The X-ray source used was a mini-focus (1 mm<sup>2</sup>) X-ray tube equipped with a W filament operating at 15 W and a Mo target. The irradiated area was 3.7 mm<sup>2</sup>, (maximum energy 30 keV) at a current of 0.5 mA. The detector was a

Peltier cooled EDS-Si with an energy resolution of 160 eV at 5.9 KeV. A user-friendly graphic interface allows the researchers to start, to stop and to save the data (Figure 3).

We used XRF spectroscopy to analyze jewelry and some rock samples, such as obsidian and pumice. For instance, obsidian was found to be made of iron (Fe) and manganese (Mn), whereas pumice is composed of iron (Fe), potassium (K) and calcium (Ca).

Moreover, we studied thirteen different pigments (from *Kremer GMBH*). The most present elements were iron (Fe), copper (Cu) and manganese (Mn). However, a very interesting target was the cinnabar (HgS) pigment (codex 10620), since it included a high quantity of mercury (Hg) (Figure 4).

We were not able to analyze the red pigment (codex 23610) because its elements were too light ( $Z<11$ ) to be investigated by the technique.

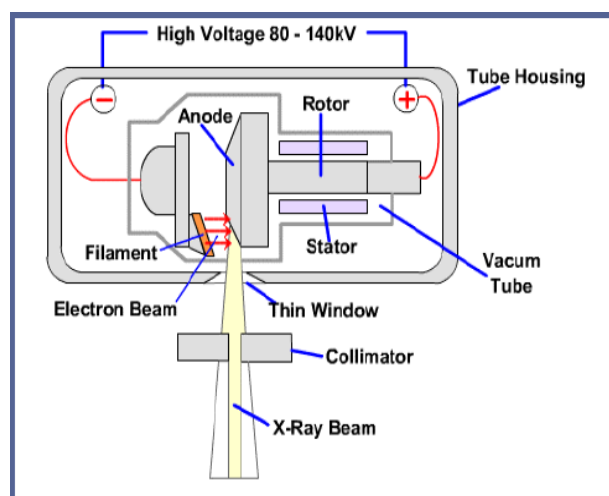


Figure 3: XRF experimental set up.

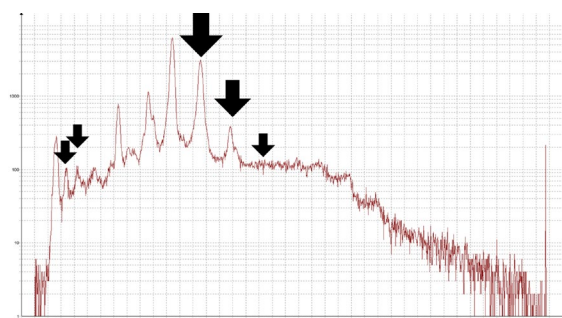


Figure 4: Cinnabar spectrum taken with XRF spectroscopy. On y axis counts, on x axis energies. Peaks are related to mercury (Hg).



## PIXE TECHNIQUE

PIXE (Particle Induction X-ray Emission) uses protons ( $H^+$ ) directly on the target to identify elements composing the sample. The machine used to run the PIXE technique was the AN2000 Van de Graaff accelerator (Figure 5).

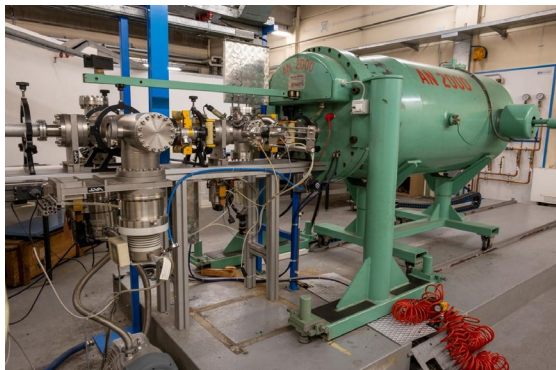


Figure 5: AN2000 accelerator.

A Van de Graaff accelerator is an electrostatic generator that produces particle beams, which can be described by electrical and magnetic laws (for example Coulomb law and Lorentz's force law). The beam goes through a channel and finally hits the target inside the reaction chamber. During the whole process the pressure inside the machine is set around  $10^{-6}$  mbar. All the parameters related to the beam can be controlled and modified remotely thanks to a linked console.

Protons, hitting the target, force their atoms to emit photons, detected by a Hyperpure Germanium (HPGe) detector, that are used to recognize the elements, from sodium (Na) to uranium (U). The Germanium detector works at the temperature of liquid nitrogen (N):  $-196^\circ C$ .

Thirteen Kremer pigments, the same colors analyzed with XRF technique, and a sample of lapislazuli were analyzed using a 2 MeV proton microbeam at the experimental station located on the beam line at 0 degrees. The typical proton current was  $\sim 3$  nA. The results gave a good confirmation of the previous analysis performed using XRF technique. Moreover, the lapislazuli showed a high percentage of sodium (Ca), sulfur (S), potassium (K) and chlorine (Cl). In Figures 6 and 7 report the elemental map of mercury (Hg) and the spectrum of cinnabar pigment, respectively. Table 1 reports the comparison of the collected data obtained by means of PIXE and XRF techniques.

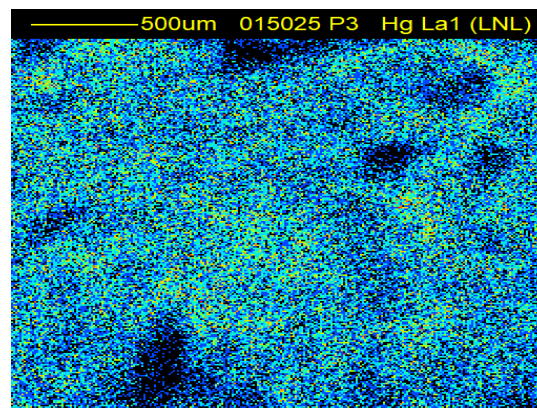


Figure 6: PIXE elemental map of mercury (Hg) in the cinnabar pigment.

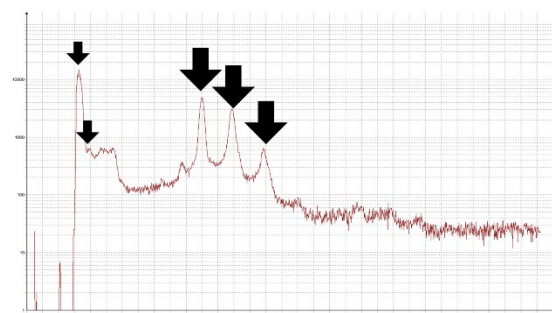


Figure 7: Cinnabar spectrum taken with PIXE technique. On y axis counts, on x axis energy in keV. Peaks are related to mercury (Hg).

Table 1: Recap of data taken with PIXE and XRF techniques. Counts under the main peaks are reported.

PIGMENT	ELEMENT	PIXE	XRF
BLUE	Fe	53343	16200
AZURITE	Cu	27934	18500
LAPISLAZZULI	Fe	3771	not analized
	S	5207	not analized
BLACK	Mn	64779	22368
INDIAN YELLOW	Co	20686	16245
	K	54142	4389
CAPUT MORTUUM	Fe	2990	21697
LIGHT GREEN	Fe	16978	19000
CINNABAR	Hg	13015	5771
TITANIUM WHITE	Ti	10219	36034
	Mn	2796	1034
RED	Cu	790	598
	Ca	408	1078
HERCULANEUM RED	Fe	9167	2473
	Ca	5158	9441
BLUTSTEIN	Fe	10762	5035
	K	6223	3196
INDIGO	Fe	1329	1390
	Cu	862	1310



## RAMAN SPECTROSCOPY

Raman spectroscopy is used to identify the molecules that compose the material. An electromagnetic radiation, emitted by a laser source, hits the targets; then, the energy spread is recorded, and the computer creates a spectrum, where each peak corresponds to a molecular bond vibration. The Raman spectra were taken using an INNORAM B&W tek portable spectrometer (785 nm and 300 mW max excitation laser) providing Raman spectra from 65 to 3004  $\text{cm}^{-1}$  with a resolution of 2.9  $\text{cm}^{-1}$ . The spectrometer uses a two-dimensional Charge Coupled Device (CCD) detector TE cooled to -20 °C to maximize dynamic range by reducing dark current. When we used this technique, we studied the pigment cinnabar, some objects (such as nacre and an obsidian stone) and a byzantine icon. The latter was the most interesting sample since it included various colors and, consequently, different materials. Even the quality of the reds was different because the shades were addressed to distinct functions (Figure 8).

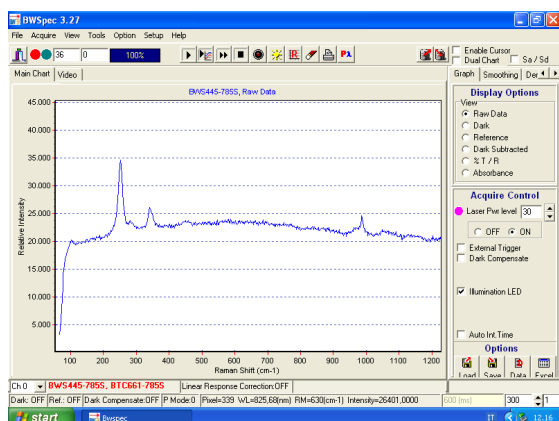


Figure 8: Raman spectrum of cinnabar during the analysis of the saint's mouth on the icon.

## RADIOGRAPHY AND TOMOGRAPHY

Both techniques use X-rays to impress a photographic plate. Whereas radiography is used for two-dimensional pictures, tomography can be used for three-dimensional reconstruction of an object.

## CONCLUSIONS

We managed to analyze the different abilities of each analytic technique thanks to different analysis technologies applied to the cultural heritage field. We later enforced these differences to create a

complete analysis of thirteen different pigments, some minerals, jewelry, and a byzantine icon to show how scientific investigation is possible regardless of the object analyzed.

## ACKNOWLEDGMENTS

We would like to thank Valentino Rigato, Davide Carlucci, Leonardo La Torre and Luisa Pegoraro. A special thought goes to Daniele Ceccato for his always available assistance and his advice.

# Neutron Time-of-flight spectrum measurement

E. Barilari<sup>1</sup>, I. Lazar<sup>2</sup>, E. Petrin<sup>3</sup>,

<sup>1</sup> *LS Volta-Fellini di Riccione, (Rimini), Italy*

<sup>2</sup> *IIS Bassi-Burgatti di Cento, (Ferrara), Italy*

<sup>3</sup> *LS Fermi di Padova, (Padova), Italy*

## INTRODUCTION

Nuclear astrophysics tries to understand the mechanisms of energy production in stars in all phases of stellar evolution and to explain the abundance of all isotopes of the elements we observe in nature. In particular, our experiment is part of the research of nuclear astrophysics because it aims to measure the neutron spectrum with the technique of time-of-flight (TOF).

The reaction  ${}^7\text{Li} (p, n){}^7\text{Be}$  is an important neutron source in the keV range and has been used in several measurements for astrophysics studies to measure neutron cross-section (CS). The cross section is the probability that a specific reaction happens. In our case, there are different reactions, but to produce our neutron we need elastic scattering, so an accelerated particle (bullet), in our case protons, interacts with a nucleus (target  ${}^7\text{Li}$ ) and create new particles as neutrons and  ${}^7\text{Be}$ . The neutron spectrum is essential for calculating the MACS (Maxwellian averaged cross-section), used in astrophysics to calculate the isotopic abundance of elements.

The technique of TOF consists in calculating the time taken by neutrons to travel a given space (flight path or FP), to calculate its speed and therefore the energy spectrum. The data obtained from the measurement will be compared with those of similar experiments carried out by Feinberg and Lederer.

## DESCRIPTION OF EXPERIMENT

The experiment was carried out at the CN particle accelerator at the Istituto Nazionale di Fisica Nucleare in Legnaro.

The CN accelerator (Figure 1) [1] a “Van de Graaff” electrostatic device, is about 7 m tall and a high voltage terminal (about 7 MV) is located at the top of the device and it’s isolated from both a tank and a gas mixture. The CN allows producing a continuous or pulsed beam of charged particles (such as protons, deuterons, and tritons or  $\alpha$  particles) through an electric field spread for the whole length. In particular, for our experiment we will use a pulsed beam of energy protons at 1912 keV. The Magnetic fields control

and focus the beam as it happens in the curvature of  $90^\circ$  at the end of the accelerator. To obtain a pulsed beam, four plates change the trajectory of the beam from a straight line

to an elliptical one and allow it to escape periodically through a diaphragm. In this way, a frequency of 3 MHz is obtained. Through a secondary pulsed beam system, placed at the end of the beamline it is possible to reduce the frequency in submultiples of 3 MHz (e.g. 1.5 MHz, 1 MHz, etc.) To obtain neutrons, we place a target of  ${}^7\text{Li}$  (Figure 2) in the path of the proton beam. Knowing the cross section of the target and the energy of the protons, we can deduct the energy of the neutrons (that varies between 0-120 keV) and the highest angle that came from the cinematic of the reaction ( $60^\circ$ ). To measure the time of flight of neutrons (nTOF) we use a lithium detector made of a scintillator, a photomultiplier, powered by a High Voltage Supplier that sends the electrical signal to the DAQ (Data Acquisition System) which allows us to analyse data with a software called Compass. The time difference between the detector detection and the pick-up located just before the target allows us to calculate the nTOF (Figure 3) from the TOF measured using the formula:

$$\text{nTOF} = \text{TOF} - (\gamma\text{TOF} - \frac{FP}{c}) \quad (1)$$

where nTOF is the real time neutrons take to move from the target to the detector, TOF is the time measured between the pickup and the detector for neutrons,  $\gamma$  TOF is the time measured between the pickup and the detector for gamma rays.

The detector (Figure 4) is a  ${}^6\text{Li}$ -glass. When neutrons interact with the detector, they can be captured and T and  ${}^4\text{He}$  particles are produced. Then the scintillator transforms charged particles energy into photons. Light is collected to a photocathode, which converts light into electrons from the equivalent energy. These electrons are accelerated and multiplied by a photomultiplier, which makes the signal readable by the DAQ.

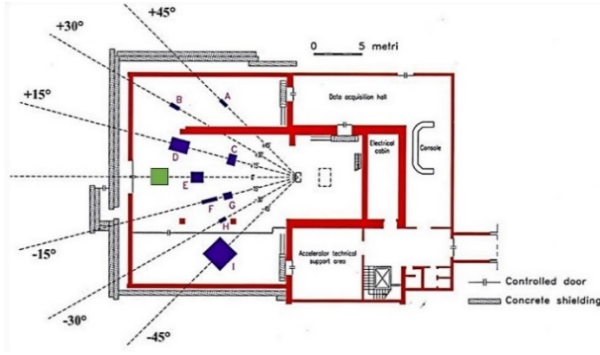


Figure 1. Floor plan of CN accelerator experimental hall.



Figure 2.  $^7\text{Li}$  target.

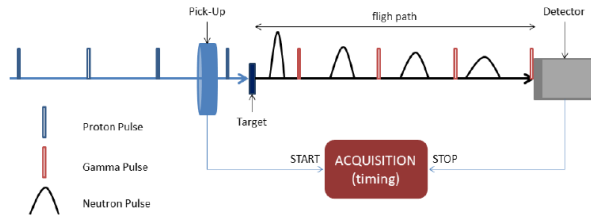


Figure 3. Time of flight method.

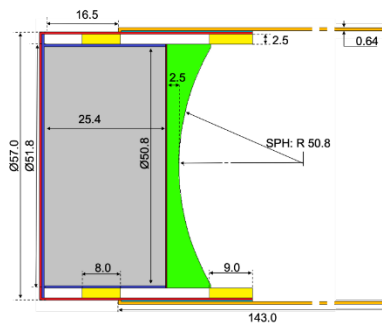


Figure 4. MC Detector

## EXPERIMENTAL SETUP

Because of the pulsed beam of protons at 1912 keV energy, the neutrons hit the target with different energy from 0 to 120 keV and the highest angle we can obtain because of the kinematic of the reaction is  $60^\circ/65^\circ$ . To take a measurement correctly, it is necessary that the  $\Delta t$  between neutrons with the highest energy and neutrons with the lowest energy when travelling through the FP is less than the T period between one proton "packet" and the next. This avoids an overlap between two different neutrons packet. This put a limitation on the frequency that we can use in the experiment. It can be increased by reducing the FP and this bring to an increase of the measurement error ( $\Delta FP=0,0128$  m;  $\Delta T=2$  ns). By reducing the frequency, so increasing the FP, the number of recorded interactions is reduced, increasing the statistical error. With some calculation, we decided the best set-up and we place the detector 72 cm from the target and produce a beam of  $f = 0,5$  MHz and current intensity between 180 and 200 nA. In this way, we can maintain an error on the measurement less than 2% and acquire a sufficient number of interactions to minimize the statistical error and obtain a valid measurement. To calculate neutrons energy ( $E_n$ ) and its error, we use the following formulas:

$$E_n = \frac{1}{2} m_n v_n^2 = \frac{1}{2} m_n \left( \frac{L}{t} \right)^2 \quad (2)$$

$$\frac{\Delta E_n}{E_n} = 2 \sqrt{\frac{\Delta t^2}{t^2} + \frac{\Delta L^2}{L^2}} \quad (3)$$

where L is the FP, t is the TOF and  $m_n$  is the neutrons mass at rest.

## DATA ANALYSIS

After taking data from our set-up, Compass software made us a 2D graphic (Figure5). This event-by-event graphic has on the ordinate the measured TOF and on the abscissa the energy of the detected particle. From this graphic, we selected the region where the energy released in the detector was higher to cut off the so-called "noise", which is the uncorrelated time background coming from cosmic rays and casual particles that hit the detector (Figure6). Then we made a TOF histogram of the previously selected events with time bins of 2 ns. Then, we measured the gamma TOF and we calculated the real nTOF using the formula (1). Then, we compared the proton spectra with a Gaussian function, and we found out that the width of our pulsed beam was around 6 ns (FWHM). Therefore, we rebuilt the time histogram with bins with a width bigger than 6 ns. As the time in the graphic increased, we had to make larger bins in

order to reach a low relative statistic error, which was around 1,4/1,5%. The final number of bins is 31, spread between 156 and 1600 ns. Then, we used a Monte Carlo simulator to produce a response matrix with 31 lines and 31 columns, which contain for every energy bin the corresponding TOF distribution (Figure 7). We calculated the inverse of this matrix and we multiplied it with the nTOF spectra. We calculated in this way the energy spectrum of the neutrons (Figure 8).

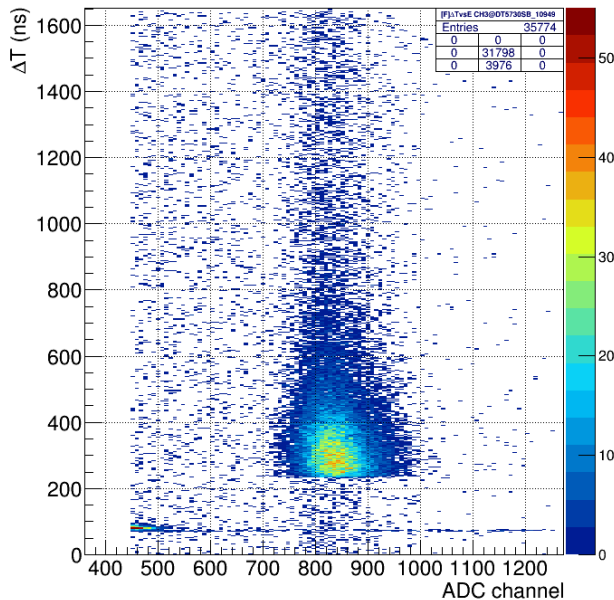


Figure 5 Compass software – 2D graphic.

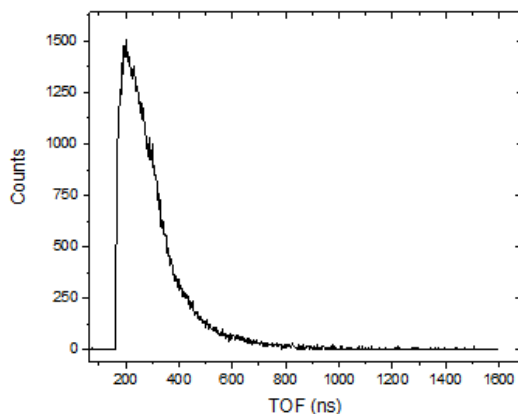


Figure 6 Neutrons TOF spectrum without background.

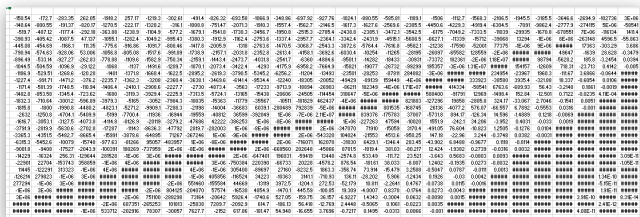


Figure 7 Inverted response matrix.

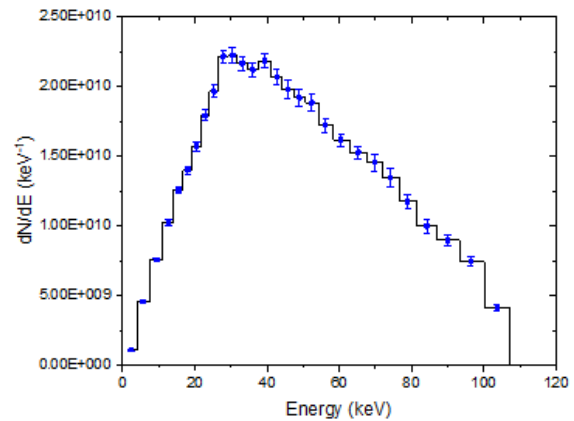


Figure 8 Energy neutrons spectrum with statistic error.

## CONCLUSIONS

We started from calculating the best experimental setup by trying to predict the best conditions for a low statistic and energetic error. Then we tested the devices used for the experiment with some gammas and neutrons sources. We organized the experiment and located the devices at the CN accelerator. We made the effective experiment, with some time issues and some problems on the beam, but we managed to collect some data. We analyzed our data using Excel and Origin software, and from the measured TOF we calculated the energy spectrum of the neutrons.

Our results came out to be different due to many problems of devices during the experiment. Firstly, we had some problems with the intensity and width of the beam. Because of this, we did not manage to make the measurement at every angle (from 0° to 60° with a difference of 10°). Then, with the few data measured, we had a bad neutron spectra and due to the short time we could not compare the results with the one made with the others detector and by other people.

## ACKNOWLEDGEMENTS

Making our experiment, the technicians, Daniele and Luca, were fundamental for the achievement. All tutors and personal were very available for every question or problem we had.

Especially we would like to thank our tutors Pierfrancesco Mastinu and Elizabeth Musacchio Gonzalez for giving us the possibility to make the experiment and patience of teaching us everything we need to understand.

## REFERENCES

- [1] <https://www.inl.infn.it/index.php/en/accelerators-3/cn>



# On Radon and cosmic rays' radiation

E. Di Carlo<sup>1</sup>, N. Ferrarese<sup>2</sup>, A. E. Mastro<sup>3</sup>, F. Prandina<sup>4</sup>, D. Toniato<sup>5</sup>

<sup>1</sup> IIS Pietro Scalcerle di Padova, (Padova), Italy

<sup>2</sup> LC Tito Livio di Padova, (Padova), Italy

<sup>3</sup> ITIS Carlo Zuccante di Mestre (Venezia), Italy

<sup>4</sup> LS Ugo Morin di Mestre, (Venezia), Italy

<sup>5</sup> LS Giorgione di Castelfranco Veneto, (Treviso), Italy

## INTRODUCTION

It is common knowledge that human beings constantly share their daily life with millions of radioactive rays, coming from both space and the underground. Mostly known for their bad reputation, radioactive rays are far from being completely understood, and this is the reason behind our study. We have narrowed the scientific research to cosmic rays (muons) and radioactive particles of Radon (isotope  $^{222}\text{Rn}$ ). The goal we aim to accomplish is to gather major information about the presence of these radioactive entities in the area of “Laboratori Nazionali di Legnaro” in Padua, Italy, to improve both the scientific knowledge on the matter and to actively help in the prevention of possible medical threats to the community.

## SECTION ONE

The noble gas Radon and its radioactive sons (such as Polonium and Bismuth) have been subject to many studies in the last few years because of the dangerous radiations they emit (the high energy particles alpha rays), which put them as the second worldwide cause of lungs' cancer.<sup>[1]</sup> The reason behind its toxicity lies in its origins: deriving from the decay of Uranium, many isotopes of Radon (as the infamous  $^{222}\text{Rn}$ ) are too unstable to survive, leading to the following decay of the particle and to the radiation of thousands of  $\alpha$  rays. While usually these rays wouldn't be considered a threat to humans, when inhaled they become increasingly dangerous, as they can modify the DNA of lungs' cells and, sometimes, leading even to cancer. These health threats are also favoured by the natural position of the gas underground, that takes advantage of its inert nature to reach houses and humans.<sup>[2]</sup>

From the many instruments that allow the detection of Radon, we have been granted the use of a “Lucas Cell”, an active method for short-period analysis. The Lucas Cell is a scintillation detector, or rather a detector of electrically charged particles, that utilizes the electrons extracted by

photons (with the photoelectric effect) that collide with a zinc film to transmit an electric signal.

We then proceeded to measure the different levels of Radon concentration in various places in the L.N.L.: office LAE, on the second floor; and the control room of the CN accelerator, located at ground level. As already asserted (figs. 1, 2), there was a relevant variation between the two locations, which can be imputed to the different levels of altitude from ground and to the distinct construction material and techniques used. Luckily enough, both data weren't, and still aren't, alarming, well below the legal limit threshold of  $300 \text{ Bq/m}^3$ ,<sup>[2]</sup> so there won't be the need for further procedures.

Figure 1

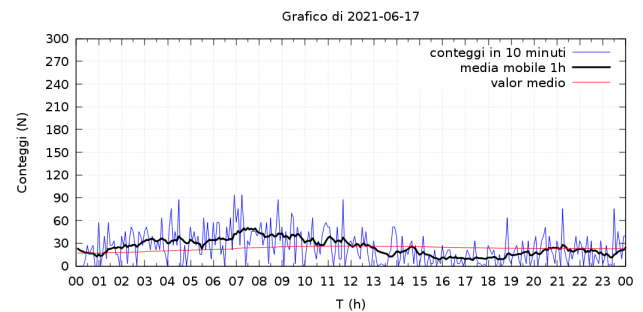
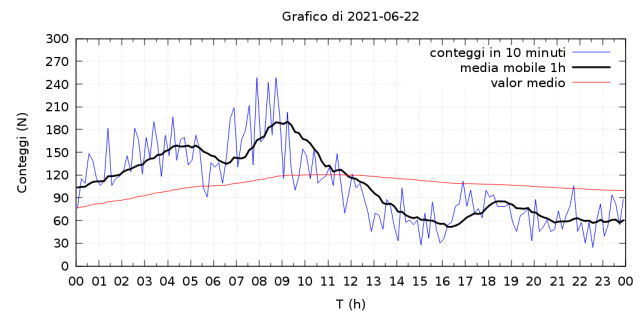


Figure 2





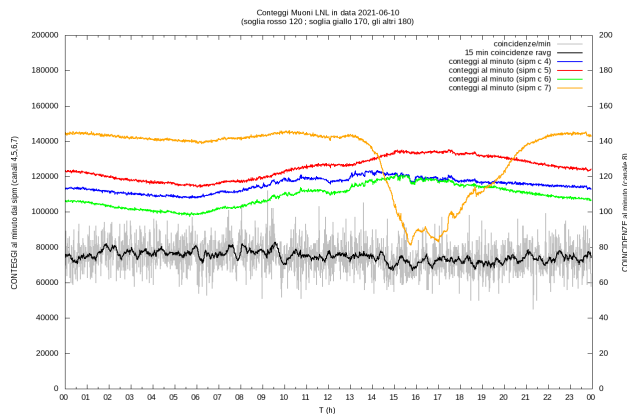
## SECTION TWO

Another field of interest for our studies are the cosmic rays, high-energy particles of solar, galactic, and extragalactic origin, the majority of which are protons. When they enter in contact with the atmosphere, these start to decay into various entities, including muons ( $\mu$ ).<sup>[3]</sup>

In order to study muons we have been granted the use of a muon detector, a scintillator consisting of a plastic plate (bc412) that emits thousands of photons when a muon passes through it. A small part of the photons (ten of ten thousand) is collected by an optic fiber and sent to a SiPM (Silicon PhotoMultiplier), which produces many electrons for each photon received thanks to polarized diodes; the signal is then pre-amplified and amplified and finally sent to be elaborated. When a signal is detected in both scintillators in a short time (in our case 50 ns), a “coincidence” occurs.

The muon detector has been active since twenty months circa. The results of these previous studies have highlighted a quite stable, but imperfect, trend of daily coincidences (76.4 coincidences per hour).

Figure 3



Nevertheless, this tendency has shown significant variations during the year, mainly because of the termic excursion and the intensity of light exposure. Taking in account these considerations, we have took measures to correct these discrepancies by changing one of the four photomultiplier's threshold of the muon detector (from 170 mV to 150 mV), and by covering up one of the scintillators with a dark material, preventing the light from interacting with the device.

For the past few months, the muon detector had been placed parallel to the ground, so that the two scintillators were perpendicular to the vertical trajectory of the majority of the muons. However, we have tried to change the inclination of

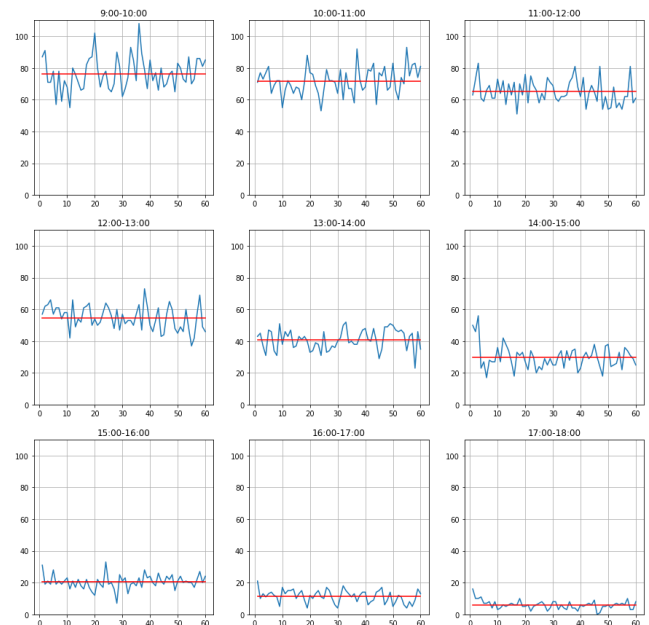
the scintillators' surface by 10 degrees per hour, with a range of 0 to 80 degrees. The results have demonstrated that most of the muons' flight is indeed vertical and not oblique, as per following data:

Table 1

Inclination (°)	Number of coincidences *	St. Dev.
0	76.43	10.27
10	71.85	8.49
20	65.05	7.59
30	54.80	7.59
40	41.00	6.37
50	29.78	7.43
60	20.48	4.36
70	11.40	3.91
80	5.93	2.67

\*(mean of coincidences per minute in a hour)

Figure 4

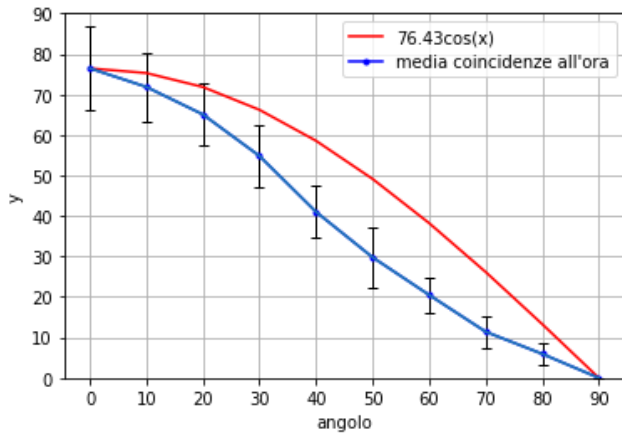


It's important to highlight that the data doesn't exactly confirm the predictions of these variations. While the muons' flow had to be proportional to the cosine of the angle defined by the perpendicular to the ground and the scintillators' plane's normal; the actual data didn't fit with

these hypotheses. The error of the measures can be imputed to the temperature's variation that occurs during the day in the detector's room, which can be the cause of misbehaviours of the electrical components.

$$\varphi_m(\vartheta) = \varphi_m(0^\circ) \cdot \cos(\vartheta)$$

Figure 6



### SECTION THREE

All the data acquired has been stored in a device for data computing, the "Raspberry pi 3". The Raspberry is a Single-Board Computer (SBC) widely used for simple data collection and analysis. The Raspberry we used had installed a Raspbian OS, a Linux distribution based on Debian OS adapted to the device.

For the first experiment, the Raspberry received the data, already in digital format, by the Lucas Cell and the plot was made using a Linux tool, Gnuplot.

In the second experiment, instead, the Raspberry was utilized for the setting of the muon detector's threshold, allowing us to obtain clearer data. The signal pre-amplified and amplified coming from the SiPM was then elaborated by an Analog-Digital Converter (since the Raspberry only works with digital data), and finally sent to the board.

We've developed a specific program, suited for the elaboration of the detectors' data. This program is written in Python language on the online platform Google Colab.

We also used these modules:

- **pandas**: for the data collection and extrapolation. For this, all the data regarding the coincidences was saved on .csv (Comma Separated Value) files.
- **matplotlib.pyplot**: to plot the data.
- **numpy** and **math**: for mathematical elaboration.

The source code, together with all the plots, is available [here](#).<sup>[4]</sup>

### CONCLUSIONS

The data and analysis shown in the article are the result of months of previous knowledge and two weeks of experiments. Those opportunities combined, allowed us to finally take some conclusions on the matter.

First, it is clear that gas Radon mainly dwells in underground space, making, as a consequence, ground floors or locals more exposed to its radiation than rooms on higher levels. We hope this further finding will sensibilize the population on the importance of the control of Radon's concentration, so that the place we call home won't become our grave.

In second place, we ascertained that temperature and light have a main role in the correct function of a muon detector (even though it wouldn't be a hazard to expand this consideration to other devices as well). Hopefully, most of the times, as in our case, the necessary adjustments aren't too difficult or time consuming.

Furthermore, the data we acquired proved the hypothesis of the prevalence of perpendicular trajectory for muons, as we have already assessed in Figure 4.

### ACKNOWLEDGEMENTS

We have for long discussed the best way to show our gratitude to the laboratories of "L.N.L. - I.N.F.N." and to our tutors Stefania Canella and Antonio Dainelli. Without their constant help and availability, we wouldn't have made much progress in the difficult path we have undertaken. The contagious passion that everyone transmitted in the laboratories has been one of the main reasons behind our excitement, and we couldn't be happier for the opportunity we have been granted. In such a predisposition of mind we end this experience, with the desire of renewing it in the future, and with the awareness that there are still people in this world that actually love what they do and that share their passion with the others.

### REFERENCES

- [1] <https://www.epicentro.iss.it/radon/epidemiologia>
- [2] <https://www.epicentro.iss.it/radon/>
- [3] <https://www.lngs.infn.it/it/raggi-cosmici>
- [4] <https://colab.research.google.com/drive/1US5bEKAX2aub5k-SYtzvN2E-Hi5f4S6v?usp=sharing>



# Radioactive Cures

H. Baggio<sup>1</sup>, E. Massano<sup>2</sup>, M. Romiti<sup>3</sup>

<sup>1</sup> *Tito Lucrezio Caro, Cittadella (Padova), Italy,*

<sup>2</sup> *Vittorio Alfieri, Asti (Asti), Italy,*

<sup>1</sup> *Giordano Bruno, Mestre (Venezia), Italy*

## SAFE OR HARMFUL?

What do you think hearing the word “radioactivity<sup>1</sup>”? As a matter of fact, this term has now entered mass culture and people are used to associate it with danger and death. Probably the first thing that comes to your mind are nuclear plants of Chernobyl and Fukushima. However, only a few people know which are the true risks, the sources, and the real benefits for man. Indeed, the first use of radioactivity occurred in the medical field at the end of 19<sup>th</sup> century. It is worth noting how radioactivity, from one hand, could damage us causing cancer and from the other it is important for the cell’s cycle.

## CANCER SOLUTION?

Nowadays there are a lot of medical applications. They range from sterilization of surgical tools to radiographic machines, such as SPECT, PET, TAC, etc.

Whereas SPECT and PET, are based on  $\gamma$  – rays , produced by the collision between a positron and an electron inside the organism, TAC works with a cathode ray tube that shoots electrons on anode. The anode overheats and emits X-rays. All these radiographic machines are useful for diagnostic purposes, to detect cancer for instance.

A further application of cancer therapy can be observed in nuclear physics laboratories: using particle accelerators where ions (electrically charged atoms) are accelerated and hurled at a target. This process creates radioactive isotopes, called radionuclide. It is bounded to a specific molecule, directed to a chosen area of the body. The radionuclide and the molecule create the radiopharmaceutical, that is used when the tumour is not surgically removable. The molecule is injected intravenously. The doctors wait until the arrive of the radiopharmaceutical in the chosen zone. The radionuclide has a half-life when it decays in different ways depending on the atom nature.

Excess of	What the atom releases	Type of decay	Examples
protons and neutrons	2 protons and neutrons	$\alpha$ -decay	<sup>226</sup> Ra
neutrons	electron (a neutron became a proton)	$\beta^-$ -decay	<sup>67</sup> Cu
protons	positron (a proton became a neutron)	$\beta^+$ -decay	<sup>62</sup> Cu
protons	X-rays (a proton capturing an electron became a neutron)	EC	<sup>125</sup> I
excited	Gamma rays	Isomer (Excited) state decay	<sup>99m</sup> Tc/ <sup>67</sup> Cu

At LNL<sup>2</sup> a group of scientists are studying a new type of radionuclide: the <sup>67</sup>Cu. Indeed, copper enters easier in cells, because it is absorbed in many cells processes, so it could be introduced also in the nucleus. Consequently, it kills more effectively tumours cells. Copper decays in two different ways:  $\beta$  and Gamma. For this reason, it might be used simultaneously both for therapy and diagnosis (theranostic purpose). To achieve <sup>67</sup>Cu scientists start from the stable atom of <sup>70</sup>Zn hitting it with protons, creating <sup>71</sup>Ga. This second element has an  $\alpha$ -decay. From this process, there is the production of <sup>67</sup>Cu and a part of <sup>64</sup>Cu left, as well. Although <sup>64</sup>Cu has a theranostic capability, doctors can inject only pure substances in human bodies.

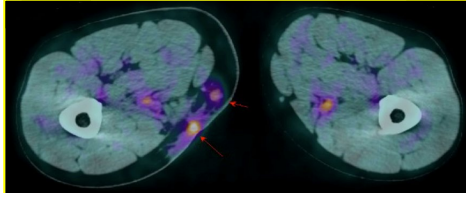
---

<sup>1</sup> the quality that some atoms have of producing a type of energy that can be very harmful to health.

---

<sup>2</sup> Legnaro National Laboratories, one building of the National Institute of Nuclear Physics.

On the left an ill organ, on the right the same after a  $^{67}\text{Cu}$  therapy.



At this phase two technical inconveniences appear: first, it is impossible to separate the two elements with chemical procedures (the two atoms seem equals), second it is too expensive as far as physical techniques are concerned.

### **A POSSIBLE HOPE?**

Now, SPES Lamared project is trying to find the simplest and cheapest way to produce  $^{67}\text{Cu}$  that could change the story of medicine. What is supposed to happen in the future?

### **ACKNOLEGMENTS**

We would like to thank:

1. Sergio Sartor
2. Laura Melendez
3. Nikolay Uzonov
4. Juan Esposito
5. Liliana Mou
6. Daniel Napoli
7. Piergiorgio Antonini

# Machine Learning for Particle Accelerator Control System

B. Bianchi<sup>1</sup>, A. Zannini<sup>2</sup>

<sup>1</sup> *LS Leone XIII, Milano (MI) Italy*

<sup>2</sup> *ITIS Zuccante, Mestre (VE), Italy.*

## INTRODUCTION

Legnaro National Laboratories (LNL) gives us the opportunity to attend a two-week stage to develop our knowledge in terms of physics and all the subjects related. There were different courses proposed and we decided to take part in “Machine Learning for particle accelerator control systems”. Our course, held by Davide Marcato and Giovanni Arena, focuses on machine learning, especially regarding its applications on accelerator control systems. The stage consists of a preliminary introduction to the Python programming language followed by the presentation of some learning algorithms, neural networks and deep learning strategies and completed by the analysis of a real use case regarding a particle accelerator.

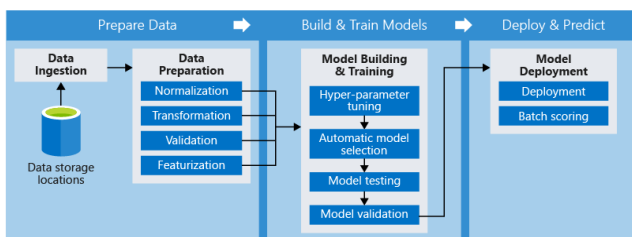
## WHAT IS MACHINE LEARNING? THE FUTURE

Machine Learning (ML) is a subset of Artificial Intelligence (AI) which uses data in order to create models, functions or algorithms to predict values. There are two types of ML: Supervised Learning and Unsupervised Learning. The main difference is that the first one learns a map from input and output data which are already defined while the second one creates a pattern from only input data. In particular we worked on Supervised Learning. It is split in Regression and Classification. In all these different types of algorithms a key aspect is the cost function: it estimates how well models are performing, comparing the real outputs and the predicted ones.

the end, we should modify the coefficients to minimise the cost. We need to be careful not to add a lot of parameters or our model can run into overfitting.

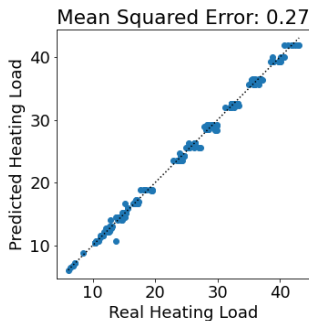
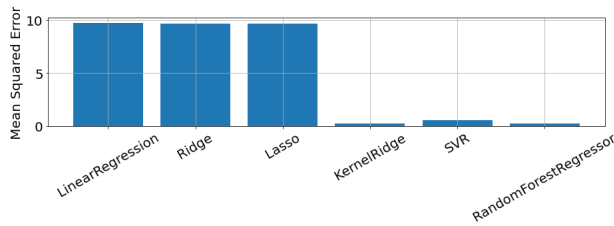
## REGRESSION

Regression consists of mathematical methods that allow data scientists to predict a continuous outcome (y) based on the value of one or more predictor variables (x). For example, you can forecast the heating load of different houses from different features such as surface area, orientation, overall height, etc. By achieving the best-fit algorithms, the model aims to predict y value such that the error difference between predicted values and true values is minimized. In this instance, the cost function corresponds with the mean squared error (MSE). It computes the square of the difference between actual and estimated values. We analysed different types of regression models: *Linear Regression* attempts to model the relationship between two variables by fitting a linear equation to observe data; *Lasso* is a model that performs both variable selection and regularization in order to enhance the prediction accuracy; *Ridge* is a model particularly useful when independent variables are highly correlated and it works in the same way of Lasso; *Kernel ridge* combines the ridge regression with the kernel trick, a simple method that projects non linear data onto a higher dimension space to make it easier to classify the data; *Support Vector Machine (SVM)* outputs a map of the sorted data with the margins between the two as far apart as possible; *Random Forest* is a meta estimator that fits a number of classifying decision trees.



This scheme describes the process followed during the creation of a model, both in Regression and Classification. First of all, we should download the data needed and prepare them through some techniques such as normalization, transformation, etc. Then, we should divide the data in two sections: train and test. The first portion is used to create the model and find the correct parameters while the second one is utilized to evaluate our model. In





$$\sum_{i=0}^n \frac{(y_i - \hat{y}_i)^2}{2}$$

\*mean squared error formula

The first graph represents the mse of every different regression model. As we can see, Random Forest is the model that works better for this problem: in this case we were trying to predict the heating load of different houses. Whereas the second graph illustrates the cost function; in this case, it is represented by a straight line where the dots represent the relationship between the real value and the predicted one.

## CLASSIFICATION

Classification is another method to predict the expected output. Compared to the regression, classification is used to categorize a set of data in different classes prearranged. Classes are also called targets or categories. For example, we tried to assign the correct target to different images of flowers using an algorithm. In this case, the cost function calculates the precision of the machine to correctly predict the classification of the data. We can have four cases which allowed to understand the capacities of our model: True Positive (Tp) which is the possibility that the machine gives the correct target to a value (in this case True), True Negative (Tn) which is the same of Tp but the answer is False, False Positive (Fp) and False Negative (Fn) which give the opposite of reality. The goal is to minimize the Fn and Fp and arrive at the best result. There is a metric that encloses the other, called F1\_Score. The model with the highest F1\_Score is the best. There are four mathematical formulas that describe the classification:

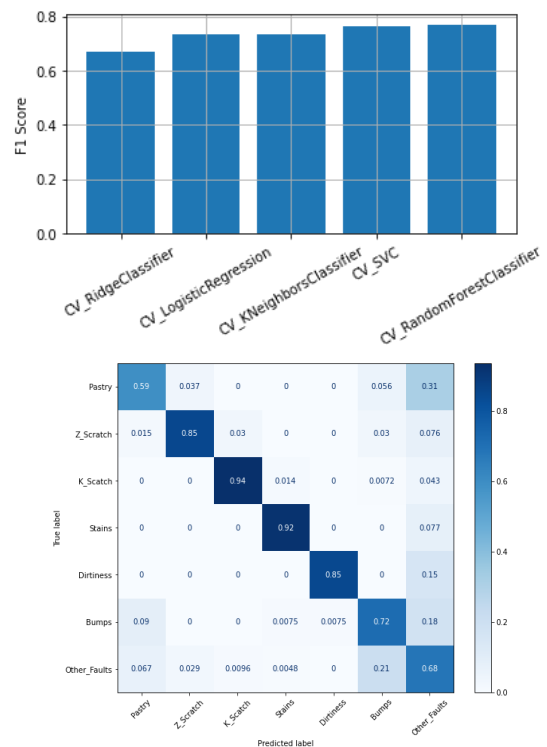
$$1) \text{ Accuracy (a)} = \frac{Tp - Tn}{P + N}$$

$$2) \text{ Precision (p)} = \frac{Tp}{Tp + Fp}$$

$$3) \text{ Recall (r)} = \frac{Tp}{Tp + Fn}$$

$$4) \text{ F1\_Score} = 2 \frac{p * r}{p + r}$$

To find the best model (the one that has the biggest F1\_Score) we applied the formula to many different classification models: *Ridge Classifier* and *Logistic Regression* work in the same way of regression; *k - Nearest - Neighbors (kNN)* is a model to classify an object in correspondence of the class most common among its k nearest neighbors, where k is a parameter that you choose independently and characterizes the model complexity; *Support Vector Classifier (SVC)* objective is returning the best fit that divides and categorizes the data; *Random Forest* is a method used also for classification that operates by constructing a multitude of decision trees at training time.

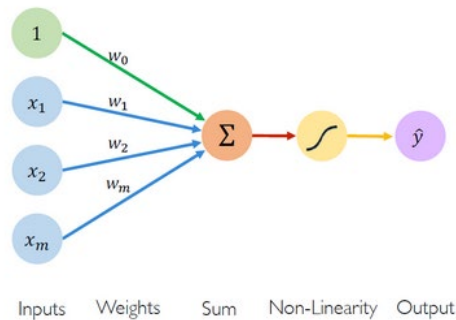


The first graph represents the F1\_Score of every different classification model. In this case, our model was trying to classify seven types of steel plate faults. We can understand that SVC and Random Forest are the best algorithms in order to solve this problem. The second

graph shows the percentages of right guessing and wrong ones.

## THE DIGITAL BRAIN: NEURAL NETWORKS

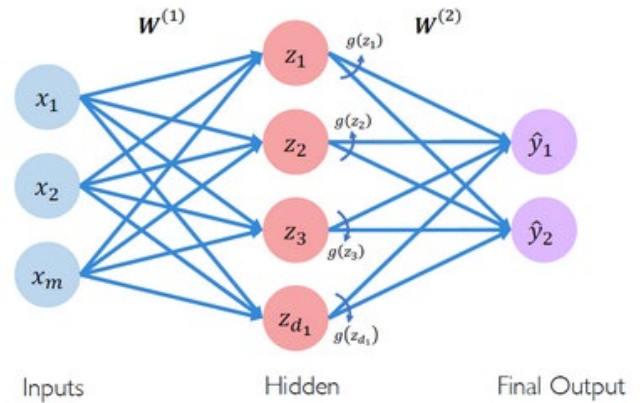
Now we start a new chapter of Machine Learning and so we must introduce a new concept: the Deep Learning (DL). Essentially the DL is a subset of Machine Learning in which multi-layered neural networks learn from vast amounts of data. It is useful because it has high performance, more autonomy, and a lot of possibilities. However, it has two main problems: the complexity and the amount of data that it needs. Like the name says, neural networks work with “digital neurons” that are explained in the photo:



Starting from the left, we can find the input data. Every data has a weight ( $\omega$ ) which is assigned by the machine automatically. The product of these two values is added up and at the total sum is applied a function chosen by the programmer. This function is called an “activation function” ( $g$ ). This process gives the output signal, which is represented by this equation:

$$\hat{y} = g(\omega_0 + X^T W)$$

It is important to remember that using a non - linear function allows us to approximate complex functions. However, we want our machine to continuously work better and handle a lot of data to give the best result. So we can add some layers. But what is a layer? Why must we add this to our neural network? A layer is a series of nodes (the quantity is of your choice) which are made up of the sum of all the products between the input data and their respective weights. After, these sums are multiplied for the activation function (that could be linear, sigmoid, rectified linear unit etc) and at the final result the machine assigns a weight that is carried to the output data. The number of layers is chosen by the programmer as well as the number of outputs.



Here are reported the formulas of this scheme:

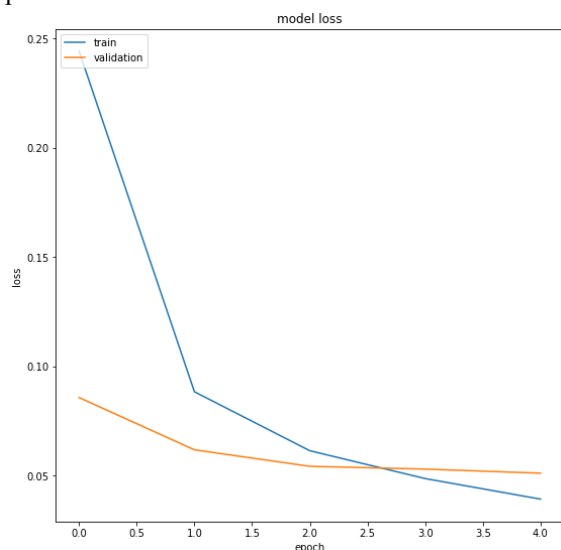
$$z_i = \omega_{0,i} + \sum_{j=1}^m x_j \omega_{j,i}$$

$$\hat{y}_i = g(\omega_{0,i} + \sum_{j=1}^m z_j \omega_{j,i})$$

## CONVOLUTIONAL NEURAL NETWORKS FOR COMPUTER VISION

These technologies are not only used for serious problems, but also to have fun. For example, everybody has tried to use Instagram or Snapchat filters to add a funny filter to a photo, for example the filter that change sex or makes you old: this is neural networks for computer vision. First, we must specify that images are made up of three different matrices standing for three different graduate scales of colours (red, green and blue). Therefore, each pixel corresponds to a number from 0 to 255. So, if we immediately apply the Flatten layer, which transforms the matrices in arrays, the spatial information is lost. For this reason, we unify neighbouring pixels using a convolutional layer. How does it work? It connects patches in the input layer to a single neuron in a subsequent layer. The result of this operation is the sum of products of the data and the respective weights. The dimensions of the sliding window are chosen by the programmer. At the end, we will have a copy of the original matrices, but smaller and deeper. After this process, we apply the Flatten layer to transform them into arrays. We have tried to use a neural network for computer vision in a program which should recognize a number handwritten between zero and nine. The train gave great results, but the test was not precise. If we put a number

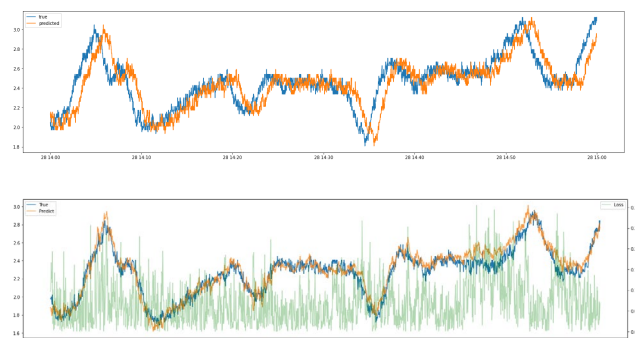
written by ourselves, the model wasn't so good, probably because the input data were grayscale images while our pictures were in black and white.



This graph represents the loss and the validation in different epochs (number of times that the computer analyses all input data). The loss, in this case the mse, is a measure of the difference between the accuracy and the perfection, while the validation is a part of training data which is used to assess the network performance. In the moment when the validation goes over the loss or starts to grow, we are in a situation called overfitting which is a problem because it means that the machines fit so much and stops being general. To contrast this problem, the model with the smallest value of validation is the best choice.

### ALPI

ALPI ("Acceleratore Lineare Per Ioni", which stands for Linear Accelerator for Ions) is a linear RF accelerator (linac), based on superconducting quarter wave resonators and used to give an energy boost to ions already accelerated by the TANDEM (a heavy-ions linear accelerator). In this course we tried to write a programming code to predict the future pressures of one of the four cryostats which are used to create superconducting working conditions. We must specify that these devices are connected and the change of pressure in one of them affects the others. So, using the data collected in a month from the first three devices, we can predict the pressure trend of the fourth. First, we had to create a baseline model: it is a dummy model which gives a result of a forecast equal to the last value. Then we calculated the mean square error of the baseline. After that passage, we generated our neural network and compared it with the MSE to see if the model is better or not. If we want to have a more precise model, we can add some layers and try to change the parameters and verify if the performance is better or not.



mse\_baseline = 0.0081

mse\_neural = 0.0066

The two graphs represent the relationship between the real pressure values (represented in blue) and the predicted one (in orange). The first one is obtained from the baseline model while the second is generated by the neural network. As we can see, the second graph is more accurate also because the mse is lower.

## CONCLUSIONS

Thanks to this course we understood the importance and usefulness of machine learning in everyday problems. In fact, we use these algorithms to forecast the heating load of different houses, to classify different images and to predict future pressures of a cryostat. We are proud to have learned something that is a hidden reality, usually studied only at university. Most people see technology only in smartphones, computers, medicine without the knowledge of a world that is enormous, because behind any function of a smartphone there is a world that includes electronics, computer technology and science. Finally, artificial intelligence will constitute the future, and it is amazing to have understood a little piece of the future.

## ACKNOWLEDGEMENTS

Davide Marcato - computer engineer  
Giovanni Arena - automation engineer

## REFERENCES

- [1] <https://archive.ics.uci.edu/ml/datasets/energy+efficiency>  
<https://archive.ics.uci.edu/ml/machine-learning-databases/00198/Faults.NNA> (classification)

# Production and test of polysiloxane scintillator for neutron and gamma discrimination

D. Boaretto<sup>1</sup>, A. Giacomelli<sup>2</sup>

<sup>1</sup>LS Ippolito Nievo, Padova (Italy)

<sup>2</sup>ITCG Cattaneo Dall'Aglio, Castelnovo ne' Monti, Reggio Emilia (Italy)

## INTRODUCTION

In this article we report on design, production and laboratory test of a polysiloxane scintillator for neutron detection.

In section one we will describe the drafting and 3D printing of the support for the double replica moulding process as well as the scintillator production.

In section two we show the performances of the scintillators under neutron and gamma irradiation.

At the end we compare our detectors with a commercial liquid EJ301 scintillator [1].

## SECTION ONE: DESIGN AND PRODUCTION

Following the double replica moulding process described in Ref. [2], we 3D printed the PolyCarbonate (PC) master with the shape shown in Figure 1 in order to obtain a truncated cone with bases with about 1 and 2 inches diameters.

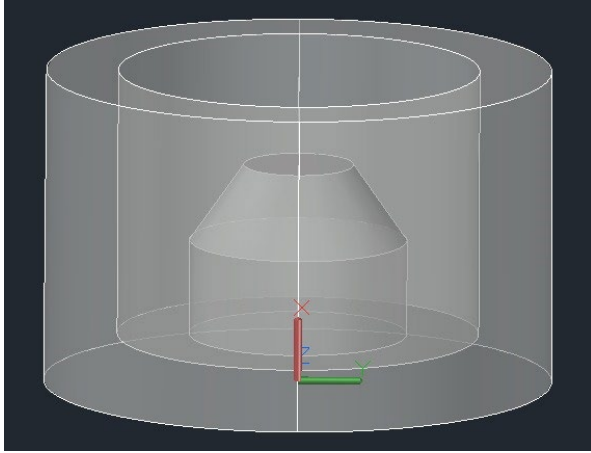


Figure 1: CAD design of the PC master

After the polishing with abrasive paper, we poured Bluesil RTV 3527 A-B silicon elastomer in the master and cured at 70° C in the oven for 15 hours. To coat this first replica with an anti-stiction layer we activated its surface in a UV ozone cleaning system for 10 minutes and vapour deposited perfluorooctyltrichlorosilane (PFOCTS) overnight. We then proceed to load the PDV-2331 vinyl terminated (22-25% diphenylsiloxane)-dimethylsiloxane copolymer with 0.02% wt Lumogen Violet (LV) and 2% wt diphenyloxazole (PPO) for one sample (A) and 1.5% wt for a second sample (B) [3].

The two samples are shown in Figure 2. Finally, we vulcanised these polysiloxane truncated cones via polyaddition and cured at 70° C during the night.

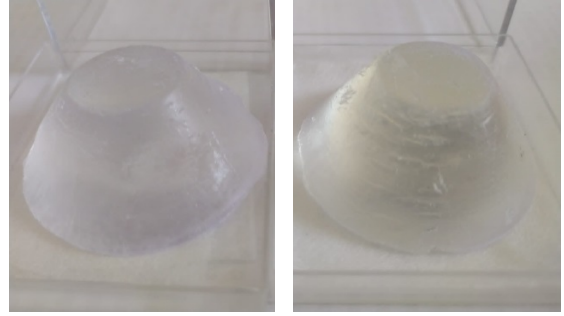


Figure 2: Sample A (left) and Sample B (right)

## SECTION TWO: LABORATORY TEST

The two samples were tested in laboratory using gamma (<sup>60</sup>Co, <sup>137</sup>Cs, <sup>54</sup>Mn) and neutron (Am-Be) sources. Their lateral surfaces were wrapped with PTFE tape and a thin aluminium foil. Their bases were coupled with photomultiplier tubes (PMT) via optical grease. We tested two configurations: for each sample we used a 1 inch Hamamatsu 6524 PMT for the upper surface and a 2 inches Philips XP2020Q PMT for the lower surface (see Figure 2). The two configurations under test are shown in Figure 3.

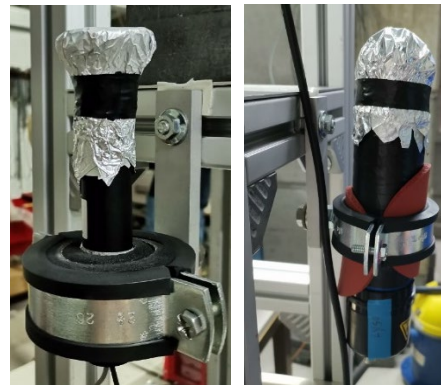


Figure 3: 1'' PMT (left) and 2'' PMT (right) configurations

The PMT signals were acquired by a CAEN DT5725 fast digitizer (250 MSamples/s, 14-bit ADC resolution and

Digital Constant Fraction Discriminator embedded in the firmware for precise timing measurements). This digitizer allows to record the PMT current pulses as digitized waveforms, to perform subsequent off-line analysis. The installed firmware can pre-process data determining the pulses timestamps and integrating them over two gates, in order to perform particle discrimination using the so-called double integration method. After the calibration of the scintillators with gamma sources we irradiated the samples with the Am-Be neutron source to evaluate gamma and neutron discrimination performances.

### SECTION THREE: ANALYSIS AND COMPARISON WITH EJ301 LIQUID SCINTILLATOR

In Figure 4 we show the 2D plot of the deposited energy vs the PSD factor which is defined as the ratio between the charge collected in the long tail of the signal and the total charge [4]. The upper line corresponds to neutron signals, while the lower one to gamma.

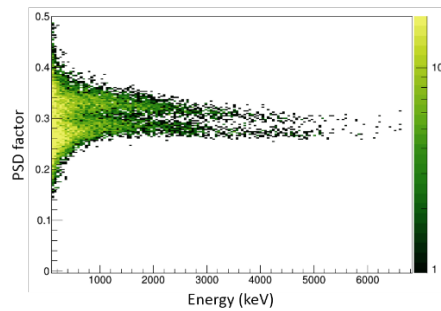


Figure 4: 2D plot of deposited energy vs PSD factor for the Sample A coupled with 2'' PMT

From Figure 4 we can see that the separation between neutron and gamma signals is improved as the deposited energy increases. To evaluate the quality of the PSD we considered the Y-axis projection for different cuts in minimum energy deposited ( $E_{cut} > 500, 1000, 2000, 3000$  keV). As an example we show in Figure 5 the PSD spectrum for the  $E_{cut} > 3000$  keV cut.

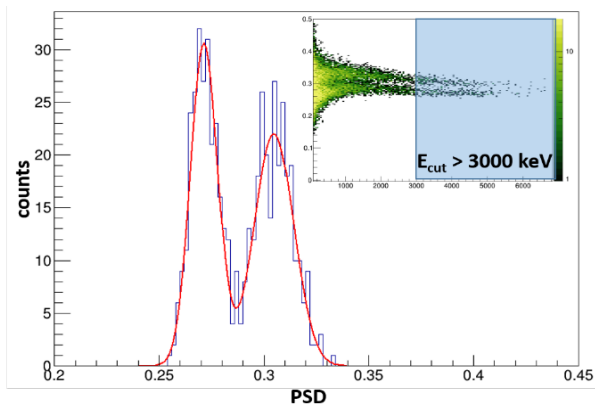


Figure 5: PSD spectrum for  $E_{cut} > 3000$  keV relative to Figure 4

For the PSD spectrum related to each cut we calculated a Factor Of Merit (F.O.M.) defined as  $(x_2 - x_1) / (\sigma_2 + \sigma_1)$  where  $x_i$  and  $\sigma_i$  are the centroids and the standard deviations of the gaussians fitting the two peaks as shown in Figure 5. A higher value of the F.O.M. means a better neutron and gamma discrimination. Finally, in Figure 6 we report the F.O.M. for different samples and configurations as a function of the energy cut  $E_{cut}$ .

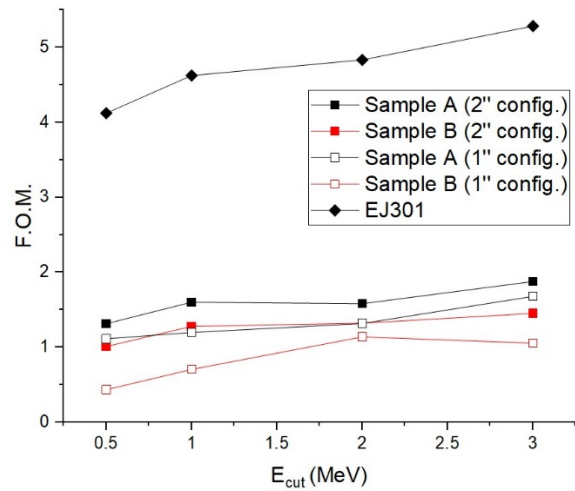


Figure 6: F.O.M. vs Energy cut for all samples and configuration. A comparison with EJ301 liquid scintillator is also shown.

From the figure we observe that the best performance is obtained with Sample A in both configurations, in particular the best results in neutron and gamma discrimination are obtained with Sample A coupled with the 2'' PMT. However, the F.O.M. obtained with our siloxane scintillators are worse with respect to a liquid EJ301 commercially available detector. In fact, it is well known that liquid materials better discriminate between gammas and neutrons.

### ACKNOWLEDGEMENTS

We acknowledge our tutors S. Bertoldo and M. Cinausero as well as G. Mantovani and F. Pino for the help in the laboratory tests. We also thank M. Sattin for the help during the 3D printing phase.

### REFERENCES

- [1] <https://www.eljentechnology.com/>
- [2] G. Zhuang and J. P. Kutter, J. Micromech. Microeng **21** 105020 (2011)
- [3] A. Quaranta et al., Mater. Chem. Phys. **137** 951 (2013)
- [4] T. Marchi et al., Scientific Report 9:9154 (2019)



# Monte Carlo method for Nuclear Physics

L. Colombo<sup>1</sup>, L. Gilli<sup>2</sup>, G. Rossi<sup>3</sup>, I. Segala<sup>4</sup>

<sup>1</sup> IIS Medi di Salò, (Brescia), Italy

<sup>2</sup> LS Ulivi di Parma (Parma), Italy

<sup>3</sup> IIS Rolando da Piazzola di Piazzola sul Brenta (Padova), Italy

<sup>4</sup> LS Galilei di Verona (Verona), Italy

## INTRODUCTION

Monte Carlo method is a statistical approach that uses random numbers to simulate the behaviour of elementary units, called events.

After generating many events, it is possible to estimate the average response of the simulated system.

This method is used in a wide range of fields, for example to predict the financial market performances or to design scientific experiments. It was also applied in the field of medical physics, for example to design diagnostic instruments with X and  $\gamma$ -rays and to estimate the effect of radiotherapy procedures.

The interaction of particles and matter is a typical problem suitable for the solution with a Monte Carlo approach. Among the Monte Carlo codes in Nuclear Physics, FLUKA [1] is one of the most used packages. In this report several simulations are presented, aiming to show the different effects and properties of particles and radiation. We will present the different behaviour of charged particles and electromagnetic radiation in water, the different outcome of the imaging applications with photons and neutrons, and the dependence of the uranium fission mass distribution from the proton energy.

## INTERACTION PARTICLE-WATER

The first set of simulations aims to study the different effects of particles interacting with water. Such material was selected to mimic the soft tissues of the human body, since they are mostly composed of this liquid.

Four different particle beams were considered, in particular:

- 80 MeV protons
- 500 KeV electrons ( $\beta$  particles)
- 80 MeV helium-4 atoms ( $\alpha$  particles)
- 0.08 MeV photons ( $\gamma$  rays)

The following graphs and plots, obtained from the FLUKA simulations, show the deposited energy per particle on the target. The beam was positioned along the horizontal axis and the water target was a 10 cm high cylinder with a 5 cm radius circular base.

### Protons-water

As we can see in Figure 1 the proton beam (the black line along the x-axis) releases more and more energy as it penetrates the target.

It deposits the biggest amount of energy when it is about to stop.

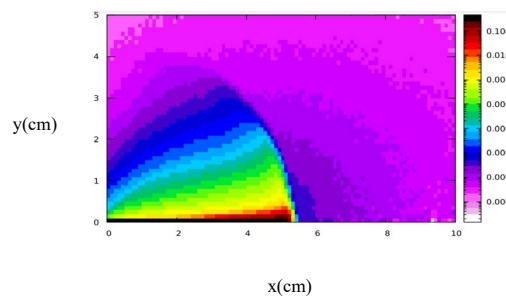


Figure 1 FLUKA simulation: energy release by proton beam in a water target (80 MeV).

We can highlight this proton behaviour thanks to an Excel chart, displaying the 1-D projection of the energy release along the beam axis:

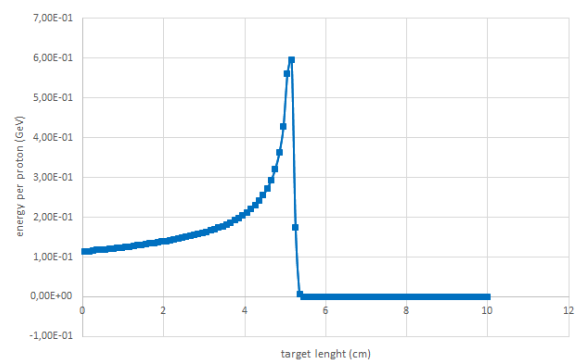


Fig 2 Excel graph: energy release by proton beam in a water target

In fact, in Figure 2 there is a high energy peak, called 'Bragg peak', when protons are about to stop. The Bragg peak is characteristic of charged particles. This trend is in agreement



with Bethe formula, from which we can draw that the energy released by the particles is inversely proportional to the square of their velocity.

### Electrons-water

As we can see in Figure 3 also electrons are stopped within the target. In such a case, the adopted electron energy (500 KeV) was lower than for the protons (80 MeV).

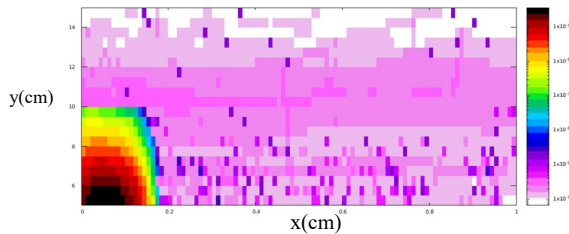


Figure 3 FLUKA simulation: energy released by an electron beam in a water target (500 KeV)

This is a reasonable energy to highlight the stopping power of electrons. Indeed, since electrons have a lower mass than protons, they tend to penetrate deeper in the matter at the same energy.

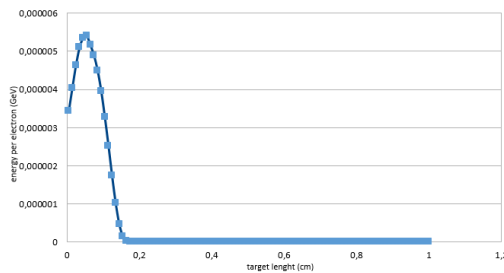


Fig 4 Excel graph: energy release by electron beam in a water target

As electrons are charged particles, they present a Bragg peak, however, since they tend to scatter, such peak is wider respect to protons.

### $\alpha$ particles-water

As we can see in Figure 5  $\alpha$  particles have a low penetration range, in fact the black line stops at the beginning of the target.

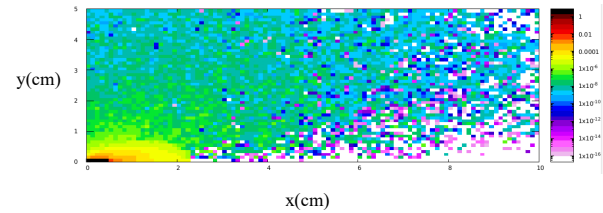


Figure 5 FLUKA simulation: energy release by  $\alpha$  particle beam in a water target (80 MeV)

Indeed,  $\alpha$  particles consist of two protons and two neutrons, therefore they turn out to be heavier than the other three particles. That is why  $\alpha$  particles are blocked more easily.

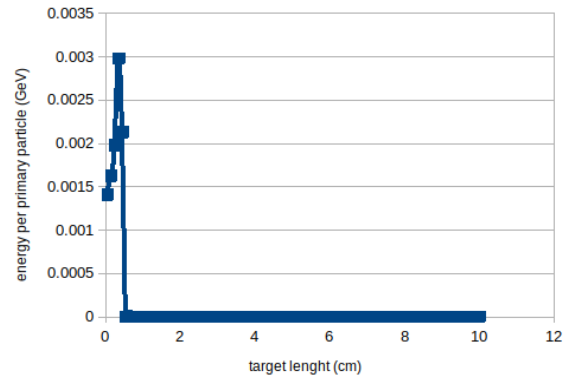


Figure 6 Excel graph: energy release by  $\alpha$  particles in a water target.

As highlighted in Figure 6, also  $\alpha$  particles exhibit Bragg peak, however, because of their low penetration length in matter, it is not as evident as in the case of protons.

In Figure 5 we can also see the effect of the secondary particles generated by the impact of  $\alpha$  with water. Indeed, such particles deposit their energy deeper in the target respect to the position where  $\alpha$  particles are stopped.

### Photons-water

As we can see in Figure 7 the release of energy by photons decreases constantly as they pass through the target.

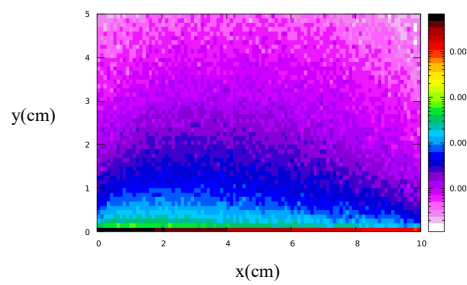


Figure 7 FLUKA simulation: energy released by a photon beam in a water target (0,08 MeV)

Photons are quanta of energy that have neither mass nor charge. Their interaction with matter depends on the material atomic number and its density. As these two parameters increase, the shielding ability of the target rises. Photon behaviour is different from the other three particles since they have no mass and no charge and because of this the way they release energy changes. We can see it also from the Excel graph in Figure 8.

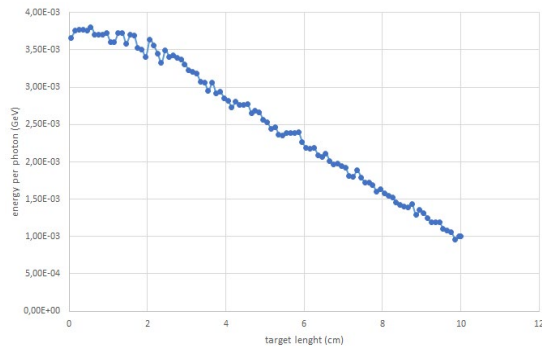


Figure 8 Excel graph: energy released by photon beam in a water target.

Indeed, we can see from Figure 8 that there is no Bragg peak. Instead of that, we can observe a constant deposited energy decrease on the x-axis.

Based on these findings, we can conclude that protons can be suitable to treat internal cancer masses since they stop in a specific position in the treated tissue, releasing a lot of energy on the cells where they are blocked. However, the proton energy should be selected carefully, as it determines the depth where the most energy is released. In fact, if the deposited energy breaks the cell DNA, also blocking any eventual repair mechanism, the irradiated tissue cells die. The simulation can be very useful to decide the suitable proton energy to ensure a damage limited only to the tumor cells.

## INTERACTION PHOTONS-MATTER

Another type of interaction particle-matter is the one that happens during a radiography. It exploits the interaction between X-rays, consisting of photons, and matter.

Figure 9 shows a closed container of aluminium which presents inside two bodies: a body of lead (the left one) and a body of bone tissue (the right one).

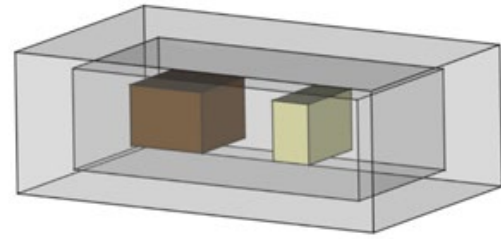


Figure 9 FREECAD [2] 3D representation: aluminium container with lead and bone tissue bodies inside.

In the Fluka simulation, such container was irradiated by photon beams (Figure 10) to observe how the two materials (lead and bone tissue) interact with X-rays.

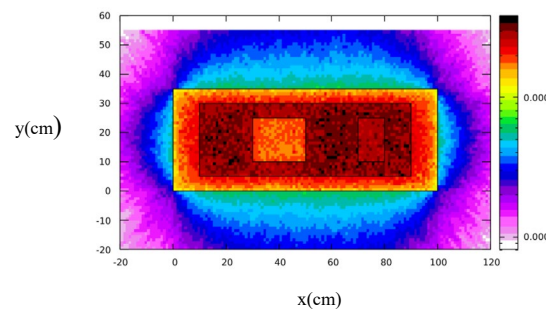


Figure 10 FLUKA imaging simulation: 10 MeV photon attenuation due to the interaction with the body represented in Figure 9

In Figure 10 we can see that lead can effectively absorb a big number of photons, which can cross bone tissue more easily. In fact, the body of lead presents lighter colours, and the body of bone tissue presents darker colours (as the darkness increases, more photons cross the body).

As we said in 'interaction photons-water', photons interact with matter depending on the density of the bodies and the atomic number of the bodies materials. The denser is the body, the more photons are absorbed.

Indeed, as shown in Figure 10, the lead holds more photons than the bone tissue, just because lead is denser than bone tissue.

For this reason, radiography, that uses low energies, is beneficial to view bone's structure and integrity. Lead, as it can absorb almost all photons, is often used as an obstacle to protect delicate areas (like gonads) from X-rays.

## INTERACTION NEUTRON-MATTER

In another case of this type of simulation, a neutron beam passed through an empty body of aluminium. This solid contained three other bodies, each one formed by a different material. In the remaining space inside of this target, there was a fifth distinct material. One run was made, and this simulation was divided in two different cases. For both of these, the number of the events (i.e. number of generated primary particles) was setted at 500 000, to obtain the most correct results as possible.

In the first case, water, carbon and iron were used as materials for the three internal bodies. To show the specific effect that the neutron beam had on each material of the three internal bodies, they were created with a different thickness, so that for every body there was the same product between the density and the thickness. Instead, the fifth material was vacuum. Moreover, the neutron beam energy was 0.01 GeV. In order to point out the number of particles that were not stopped by the different materials, only one userbin card was used, specifying his position outside the aluminium body on the opposite side from the beam source.

Because of this, we can understand how the various bodies interact with the neutron beam. As it is possible to see from the 2D graph (Figure 11), the neutrons were mostly stopped by less dense materials.

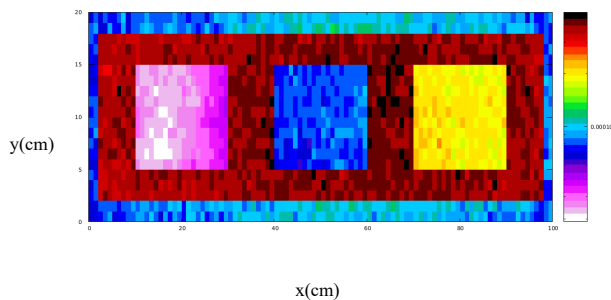


Figure 11 FLUKA imaging simulation: amount of detected neutrons in a determined geometry

In fact, in the first two bodies from the left (respectively formed by water and carbon), there are colors that are in the low part of the scale (which is at the right of the chart). Instead, in the third body (formed by iron), there are colors that represent higher amounts of particles. Also, we can see that aluminium stops not many particles and obviously the vacuum does not stop anything. In the second case, the same materials and parameters were used, the only difference was the type of graph considered. Indeed, the 1D graph was examined (Figure 12), to see if in one dimension the results were the same as in two dimensions.

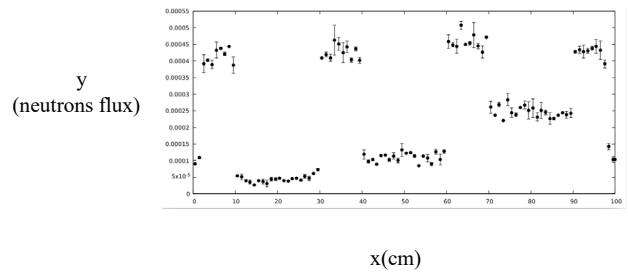


Figure 12 FLUKA imaging simulation: amount of detected neutrons along the x axis

As we can notice from the graph, there was an acceptable range of error, thanks to the number of events chosen. Besides, the values obtained respect the geometry created and were the same as in 2D.

So, we can conclude that it is proved that neutrons are better stopped by less dense material, as this type of particle interacts more with that type of material.

## PROTON INDUCED FISSION ON URANIUM-238

A particular type of interaction particle-matter is the one between protons and uranium-238. When a uranium-238 target is irradiated with a proton beam, the fission reaction is induced. It means that uranium atoms split, generating two nuclei belonging to lighter elements.

Through the Monte Carlo code Fluka and a subsequent data processing using Microsoft Excel, it was possible to create a graph displaying all the different produced nuclides by the uranium-238 fission.

The following graphs show the produced amount for each nuclide normalized per proton.

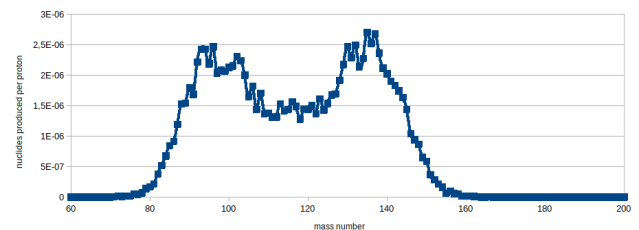


Figure 13 Excel graph: nuclides produced per proton by U238 fission (35 MeV)

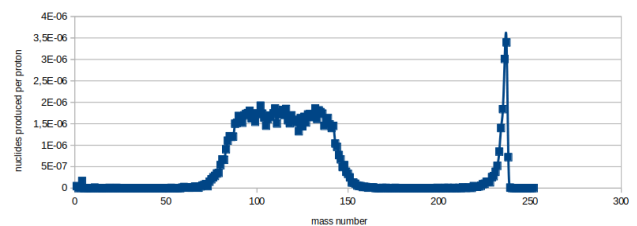


Figure 14 Excel graph: nuclides produced per proton by U238 fission (200 MeV)

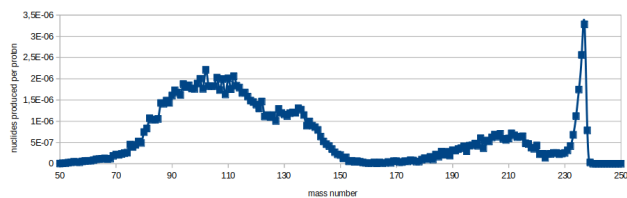


Figure 15 Excel graph: nuclides produced per proton by U238 fission (1 GeV)

From Figure 13 we can see that with low energies the graph curve presents two evident peaks which merge as the energy increases. This means that with lower energies it is more probable that uranium-238 splits into two nuclides one heavier than the other (the left peak indicates low mass numbers of nuclides, the right one indicates high mass number nuclides).

Quite the opposite, from Figure 15 we can see that with high energies it is more probable a uranium-238 core splits into two nuclides having similar mass numbers.

Therefore, with low proton energies the mass distribution of the fission products is asymmetrical, while with high energies it becomes more and more symmetrical.

It is interesting to highlight that with high energies (Figure 14 and Figure 15) also other reactions occur, we can observe another nuclear reaction peak (spallation) at masses around 220 - 240 amu.

## CONCLUSIONS

In this report we had analysis different type of interaction between particles and matter:

- Protons-water
- Electrons-water
- $\alpha$  particles-water
- Photons-water
- Photon-matter
- Neutron-matter
- Uranium-238 fission

Monte Carlo methods can be used in different Nuclear Physics fields. They are very useful because, through such simulations, you can predict the outcome of experiments making it less uncertain.

## ACKNOWLEDGEMENTS

We also want to thank our tutors Michele Ballan and Luca Morselli for having accompanied us on this journey and for teaching us so much.

## REFERENCES

- [1] <http://www.fluka.org>
- [2] <https://www.freecadweb.org>



# Silicon Photomultiplier Characterization

L. Alessandrino<sup>1</sup>, N. Buttini<sup>2</sup>, S. Busatto<sup>3</sup>

<sup>1</sup> LS G. Cotta di Legnago, (Verona), Italy.

<sup>2</sup> LS G. Veronese di San Bonifacio, (Verona), Italy.

<sup>3</sup> LS G. Ulivi di Parma, (Pr), Italy.

## INTRODUCTION

Through the CAEN kit it is possible to conduct lots of experiments of diverse nature. They can concern different particles and radiations, including photons, muons,  $\gamma$  and  $\beta$  rays that are transformed in light through a scintillator to be detected by a Silicon photomultiplier. Our experience focuses on the first. The task of the experiment was to use a primitive Photon Counting (PC) to characterize our SiPM (silicon photomultiplier).

## SILICON PHOTOMULTIPLIER (SiPM)

The SiPM, composed by a dense array of small, independent SPAD sensors, wired in parallel (see Figure 1). Every microcell has a quenching resistor, that is necessary in order to block the avalanche current and to reset the cell itself. This phenomenon is generated through a photodiode, an optical sensor that recognizes photons with a specific wavelength, then it converts them into the avalanche generation of electron-hole pairs, our current. The photodiode allows the amplification of the charge by a factor of  $\sim 10^6$ .

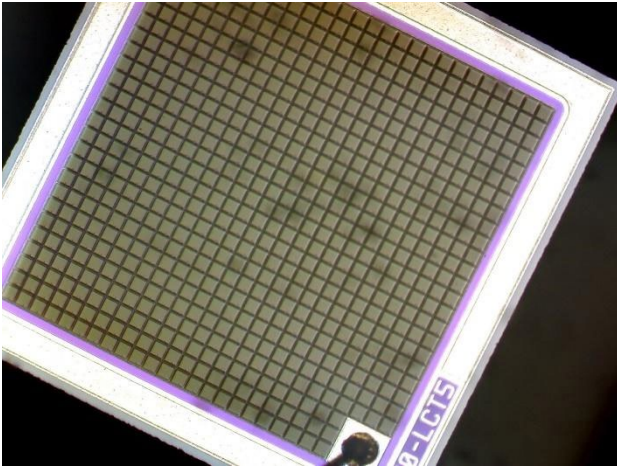


Figure 1. Picture of the SiPM “Hamamatsu s13360-1350CS” obtained through an optical microscope.

The SiPM is a Silicon photomultiplier, composed of a dense array of small, independent SPAD sensors, wired in parallel. The SiPM can provide an ultra-fast output signal. This fast output signal is generated by the fast switching of the microcell right after the detection of a single proton. This signal allows higher count rates, the capability for second

photon timing and can be used for ultra-fast timing measurements.

## INSTRUMENTS

-LED Driver (purple light generator,  $\lambda = 400\text{-}410\text{ nm}$ ): Typical wavelength 405 nm, width of pulse 8ns typical at full amplitude, Output frequency from 500 Hz to 5 MHz

-Optical fiber

-PSAU (Power Supply e Amplificator): Gain 0-50 dB, step 1 dB

-Digitizer (ADC: analog-to-digital converter). Analog input: 2 channels, impedance 50  $\Omega$ , Full scale range 2 V<sub>pp</sub>. Digital conversion: resolution 12 bits, sampling rate 250MS/s on each channel simultaneously. Trigger Source: self-trigger that activates when the channel is over or under threshold for common (waveform recording firmware) or individual (DPP firmware only) trigger generation; external-trigger which is a common trigger by TRG in connector or individual by LVDS connector; Software-trigger, which is a common by software command.

-Computer (CAEN software: HERA / SiPM control software)

-Hamamatsu SiPM: Effective photosensitive area 1.3 x 1.3 mm, Number of pixels 667, fill factor 74%. Measurement conditions: V<sub>over</sub>= 3V, typical dark count 90 kcps, breakdown voltage V<sub>br</sub> 53 $\pm$ 5.

## EXPERIMENTAL PROCEDURE

The light pulse from the LED driver is driven through an optical clear fibre into the SiPM and connected to the PSAU. Then the amplified signal from the latter is conducted into the input of the DGTZ. Both modules are connected via USB to the computer.

To interpret the digital signal a software called “SiPM Control Software” is used. To show the signal represented in Fig 4, as well as other parameters and plots which will be discussed later, it is necessary to regulate the PSAU and the



DGTZ the values shown in Fig 2.

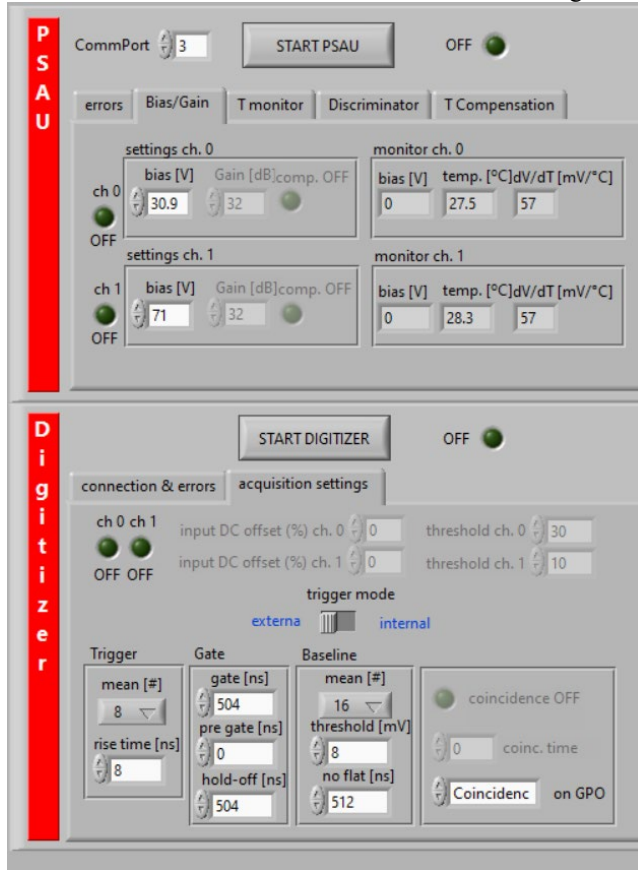


Figure 2. control panels for the DGTZ and the PSAU

On the PSAU panel it is possible to regulate 2 parameters per channel: a BIAS voltage and a GAIN. The first serves the purpose of biasing the PM, running a current across the whole component from an anode to a cathode. This parameter is versatile: as shown in Figure 3.

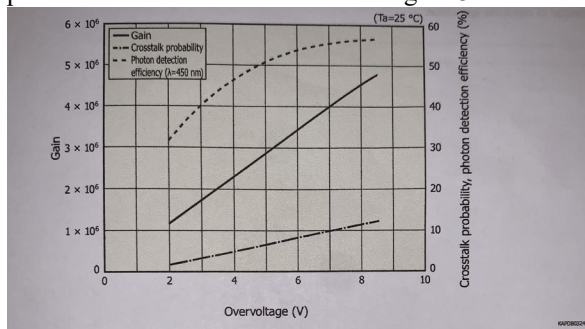


Figure3. Variation of gain and efficiency upon an overvoltage application

The overvoltage is the amount of voltage that is given to the SiPM over its required  $V_{br}$ . The main advantage is the linear increase in gain that can be produced before passing through the gain stage in the amplifier, while the drawbacks are multiple: too much overvoltage increases the DCR and crosstalk probability, threatening the accuracy of the measurements.

To have a more precise and controllable amplification the PSAU has an amplifier that steps up the gain of the signal from 0 to 50dB maximum, with no particular drawbacks.

The DGTZ has more parameters that are shown in Figure2 and in Figure4 are applied to the graph. The red line indicates the “Gate” or the interval in which the integration is carried out. It can be regulated in width, with gate and pregate parameters, and can be set to stop the calculations after a certain time span, which is the hold-off. The green line shows the “Baseline” which is an average of the samples of the input signal in flat condition, and the white line represents the pulses coming from the SiPM.

The LED driver generates a TRIGGER signal for starting the digitalization, which can be used switching the trigger mode to external and plugging the trigger cable from trigger out to the trigger in of the DGTZ.

The software is launched, and the data is acquired. A typical measurement is shown in Fig 4.

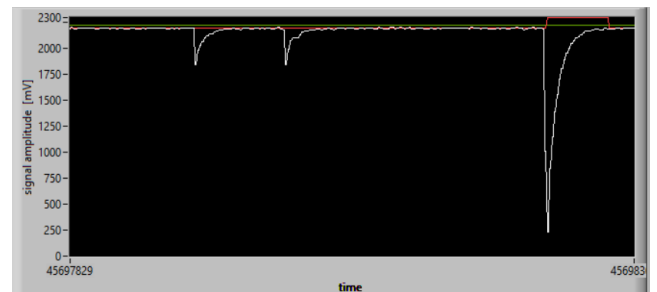


Figure 4. Shot of a momentary peak detected by the SiPM.

The curve seen in the figure 4 represents the voltage variation provoked by the outputs of the single cells summed together, in time intervals.

The main source of noise in a SiPM is the Dark Count Rate (DCR) which is mainly caused by thermal electrons. The signals generated by these thermal electrons are identical to the signals produced by photons. Therefore, the thermally generated electrons are a source of noise at the single photon level.

The peaks seen in the graph shown in Figure4, could then be partially generated by some thermal noise.

To prevent this from interfering with measurements, PSAU gain can be augmented as well as the signal magnitude.

## DATA ANALYSIS

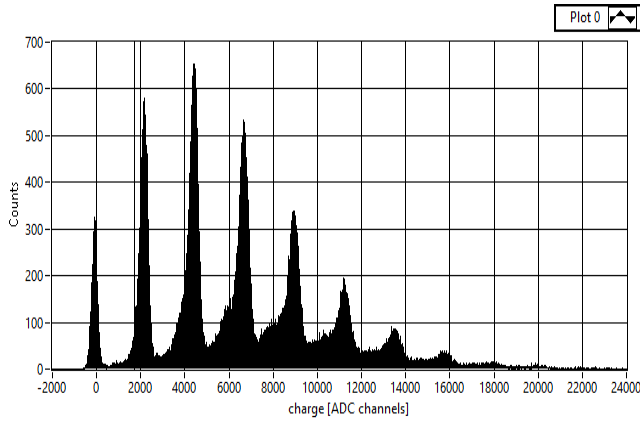


Figure 5. Histogram of the photoelectrons outputting a charge.

What is represented in Figure 5. is a statistical trend of the photons hitting the various cells. The X axis has a dimension expressed in ADC (ch). The ADC (ch) is the minimal surface unit read by the DGTZ in an 8 ns time interval. As already reported, the DGTZ used has a resolution of 12 bit so it can divide an integrated area in 4096 sectors with a sampling rate of 8 ns.

$$ADC_{ch} = \frac{V_{pp}}{R_0} \cdot \frac{dt}{2^{12}} = \frac{2V}{50\Omega} \cdot \frac{8ns}{2^{12}} = 80 fC/ADC_{ch}$$

2V is the maximum voltage that the DGTZ can read before the signal clips,  $50\Omega$  is the impedance opposed by the DGTZ, to let a current pass.

The value above represents the “maximum sensibility” that the DGTZ can provide.

## CONCLUSIONS

While the number of peaks rises, the space between them ( $\Delta_{pp}$ ) remains constant, so the plot reflects a Poissonian trend: this means that the photons generated by the LED driver are uniformly distributed and independent from each other.

## ACKNOWLEDGEMENTS

Dott.sa Mattone Cristina (CAEN assistant)  
 Prof. Menozzi Roberto (UNIPR professor)  
 Dott. Gianluigi Maggioni (INFN LNL)

## REFERENCES

- [1] Digital pulse processing for SiPM Kit; preliminary user's guide.
- [2] G. Galletta., Risoluzioni energetiche e temporali di rivelatori SiPM, Cap 1, Master Thesis, Università Bari, 2012.
- [3] ON semiconductors, Introduction to the silicon photomultiplier  
<https://www.onsemi.com/pub/Collateral/AND9770-D.PDF>

